People's Democratic Republic of Algeria
Ministry of Higher Education and Scientific Research

University M'hamed Bougara Boumerdes
Institute of Electrical and Electronic Engineering
Department of Electronics

Final year project report presented in partial fulfillment
of the requirements for the degree of

MASTER

In **Power engineering**
Option: **Power**

Title:

Comparative simulation study of CdS/CIGS and CdS/CZTS solar cells

Presented by:

- **SAIDI Yasser Abderrahmane**
- **BADAOUI Abdelkarim**

Supervisor:

Dr. CHALA Slimane

Registration number /2024

ACKNOWLEDGMENT

*We would like to express our sincere gratitude to our supervisor***, Dr. CHALA Slimane***, for his invaluable guidance and support. His willingness to take the time to orient us was instrumental in our success.*

We would also like to extend our thanks to the esteemed members of the jury who will be attending my presentation. Their insights and feedback are highly anticipated.

Finally, we would like to thank the entire administrative staff of the university for their dedication and hard work in fostering a supportive learning environment.

DEDECATION

To our families, the unwavering pillars of support. Your endless love, patience, and encouragement fueled our determination throughout this journey.

This project is a testament not only to our hard work but also to the sacrifices you made to see us succeed.

We are deeply grateful for your unwavering belief in us.

ABSTRACT

This work represents a comparative study using Silvaco-Atlas numerical simulation software to analyze the IV photovoltaic characteristics of two thin-film solar cells, ZnO/CdS/CIGS/MO and ZnO/CdS/CZTS/MO. The study aims to find the optimal thickness and doping concentrations for the CdS, CIGS, and CZTS layers to maximize the efficiency of CdS/CIGS and CdS/CZTS solar cells and compare their performance. The research is motivated by the need to explore and optimize solar energy solutions to better meet energy demands. By using Silvaco-Atlas simulations, the study determines the best parameters for these solar cell configurations. The optimal IV parameters for CdS/CIGS were found to have a higher short-circuit current density and overall efficiency, with specific thicknesses and doping concentrations for the CdS and CIGS layers. For CdS/CZTS, the best IV parameters showed a higher open-circuit voltage and fill factor, with certain thicknesses and doping concentrations for the CdS and CZTS layers. In comparison, CdS/CIGS solar cells exhibited higher short-circuit current density and efficiency, while CdS/CZTS solar cells demonstrated higher open-circuit voltage and fill factor. This indicates that while CdS/CIGS cells are more efficient overall, CdS/CZTS cells have potential advantages in specific performance metrics such as open-circuit voltage and fill factor.

SUMMARY

Chapter 1: Type Of Materials

Chapter 2: Solar Cells

Chapter 3: Simulation Methods

Chapter 4: Results And Descussion

LIST OF FIGURES

Chapter 1: Type Of Materials

Chapter 2: Solar Cells

Chapter 3: Simulation Methods

Chapter 4: Results And Descussion

LIST OF TABLES

Chapter 3: Simulation Methods

Chapter 4: Results And Descussion

LISTE OF ABREVIATIONS

1. CIGS: Copper Indium/Gallium Selenide
2. CdS: Cadmium Sulfide
3. CZTS: Copper Zinc Tin Sulfide
4. SILVACO: Silicon Valley Corporation
5. ZnO: Zinc Oxide
6. VWF: Virtual Wafer Fab
7. TCAD: Technology Computer Aided Design
8. Mo: Molybdenum
9. FF: Fill Factor
10. Eg: Optical Band Gap
11. E: Energy
12. η: Solar Cell Efficiency
13. α: Absorption Coefficient
14. λ: Wavelength of Diffraction
15. EF: Fermi Level (eV)
16. T: Temperature (K)
17. n: Electron Concentration (cm^{-3})
18. ni: Intrinsic Carrier Concentration (cm^{-3})
19. P: Hole Concentration (cm^{-3})
20. Ec: Lower Level of the Conduction Band
21. Ev: Upper Level of the Valence Band (eV)
22. Dn: Electron Diffusion Coefficient (cm$^{2}\cdot$s^{-1})
23. Dp: Hole Diffusion Coefficient (cm$^{2}\cdot$s^{-1})
24. Nc: Density of States in the Conduction Band (cm^{-3})

25. Nv: Density of States in the Valence Band (cm^{-3})

26. h: Planck's Constant (6.62×10^{-34} J·s)

27. A: Material Constant

28. ε: Dielectric Constant

29. Iph: Photocurrent (mA)

30. Voc: Open-Circuit Voltage (V)

31. Isc: Short-Circuit Current (mA)

32. Jsc: Short-Circuit Current Density (mA/cm^2)

33. IQE: Internal Quantum Efficiency (%)

34. k_B: The Boltzmann constant

35. N_B: The number density of the background carriers

GENERAL INTRODUCTION

A solar cell, or photovoltaic (PV) cell, is an electrical device that converts the energy of light directly into electricity by the photovoltaic effect. It is a form of photoelectric cell, defined as a device whose electrical characteristics vary when exposed to light.

The primary objective of the worldwide PV solar cell research and development is to reduce the cost to a level that it will be a viable alternative to conventional ways of generating electric power. PV technology in the marketplace today is dominated by crystalline silicon. It is generally believed that even with greatly increased market and production volume, the price of crystalline or polycrystalline silicon cannot be reduced to meet the long-term cost goal for large scale power production. In fact, various analyses suggest that thin film solar cells are the only viable alternative that has the potential to meet this long-term cost goal by reduce the quantity of semi-conductor materials used in the composition of each cell and increase its lifespan. If one accepts this rationale, it is instructive to analyze whether thin film technology can realistically meet these goals. There is reason to be very optimistic, particularly in view of the remarkable progress that has been made in recent years, both in terms of cell efficiency and long-term stability in several thin film solar cell technologies.

Because of the high costs of experimentation, researchers have moved towards the use digital simulation software such as SILVACO to predict the response of structures based on materials prepared for photovoltaic conversion. This software allows hundreds of parameter combinations before the actual manufacturing of the device. It's a fast, consistent and inexpensive way to design solar cells. It allows, among other things, visualization of the parameters that influence the behavior of solar cells. The objective of this present dissertation is the study by numerical simulation of the solar cell.

We will simulate the effect of the thickness and doping of the CdS with CIGS and CZTS layers in order to optimize the solar cells.

To do this, our work is divided into four chapters as follows:

- **Chapter 1:** We will present the physical properties of semiconductors in general and the CIGS semiconductor in particular constituting the solar cell.

- **Chapter 2:** A study on solar cells in general, we will also describe the operating principle and the characteristics of these solar cells.
- **Chapter 3:** We will present the Silvaco software uses for the simulation of the cell solar.
- **Chapter 4:** And finally, In the last chapter we will present and discuss the results obtained.

CHAPTER 1

TYPE OF MATERIALS

1.1. Introduction:

The majority of modern solar cells rely on semiconductor materials for the absorption of photons, which produces charge carriers, and the subsequent separation of the charge carriers that are formed by photosynthesis. As a result, the most crucial components of a solar cell are the semiconductor layers. For the purpose of converting photon energy into electrical energy, a variety of semiconductor materials are appropriate; each has pros and cons.

1.2. Materials classification:

The orbit in which an electron revolves determines the energy of that electron in an isolated atom, according to the Bohr atomic model. However, if atoms are originally arranged in a regular periodic pattern and then pushed closer together, the initial quantized energy level will break into a band of discrete energy levels [1], [2].

There is a band of permitted energies at the equilibrium interatomic distance, but the energies are at discrete levels within the allowed band. According to the Pauli Exclusion Principle, regardless of atom size, uniting them to form a system (a crystal) does not change the total number of quantum states. But for each electron to occupy a unique quantum state, the discrete energy needs to be split into a band of energies because no two electrons can have the same quantum number [2].

Once more, consider an atom arrangement that is regular and periodic, with many electrons present in each atom. The electrons in neighboring atoms won't interact and will occupy the discrete energy levels if the atoms are originally quite far apart. This discrete energy level will break into a band of permitted energies if these atoms are pushed closer together because the outermost electrons in the $n = 3$ energy shell will initially start to interact. The electrons in the $n = 2$ shell may interact and split into a band of permitted energies if the atoms continue to approach one another. The innermost electrons in the $n = 1$ level may finally interact if the atoms reach close enough to one another, splitting this energy level into a band of permitted energies as well. In Figure 1.1 [2], the splitting of these discrete energy levels is qualitatively depicted.

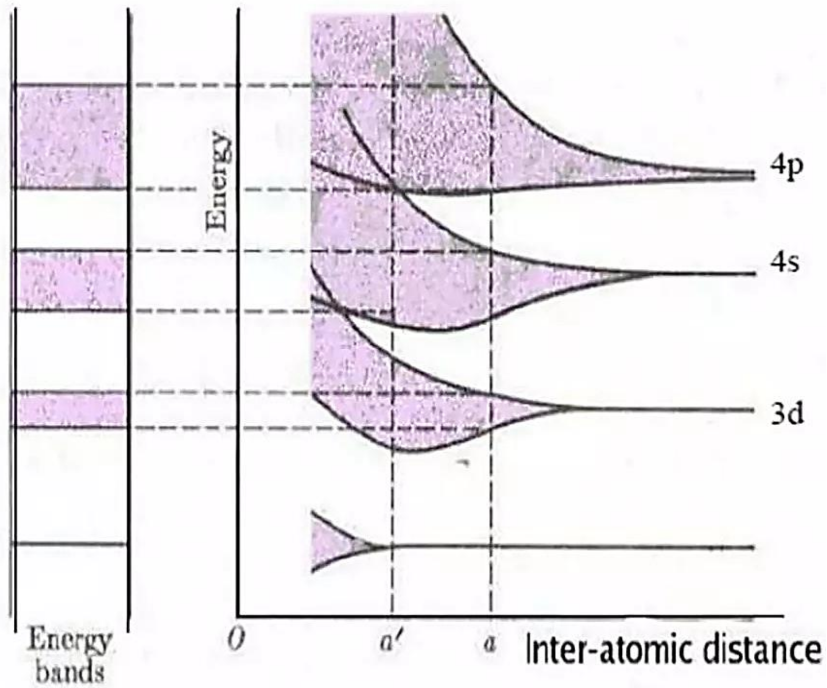

Figure 1.1: Schematic showing the splitting of three energy state into allowed bands of energies.

We have bands of permitted energy that the electrons may occupy, divided by bands of forbidden energies, if the equilibrium interatomic distance is r0. The energy-band theory of single-crystal materials describes this splitting of the energy band and the creation of allowed and prohibited bands. The real band breaking in a crystal is far more intricate, as Figure 1.1 illustrates. The silicon band splitting is depicted in Figure 1.2. For the valence electrons, we only need to take into account the n = 3 level because the first two energy shells are fully occupied and firmly bonded to the nucleus. There are two quantum states per atom in the 3s state, which is equivalent to n = 3 and l = 0. At T = 0 K, there will be two electrons in this state. There are six quantum states in each atom of the 3p state, which is equivalent to n = 3 and l = 1. In this state, the final two electrons will be present in each silicon atom. The 3s and 3p states interact and overlap, resulting in a decrease in the interatomic distance. The bands have once again separated at the equilibrium interatomic distance; however, each atom now has four quantum states, four in the upper band and four in the lower band [2].

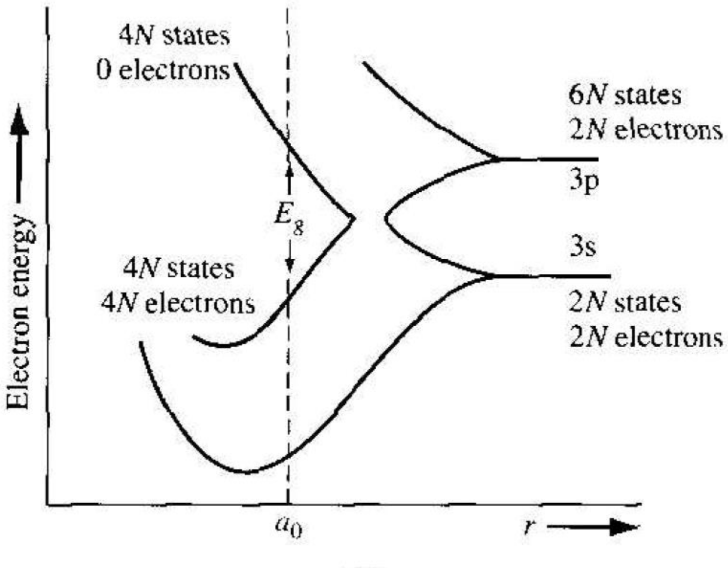

(b)

Figure 1.2: Formation the allowed and forbidden energy bands.

Since electrons are in their lowest energy state at T = 0 K, all states in the valence band, which is the lower band, will be filled, and all states in the conduction band, which is the upper band, will be empty. The symbols EC and EV represent the lowest and greatest energy levels, respectively, in the conduction and valence bands. There are many closely spaced energy levels above EC and below EV. The energy band gap (Eg) is the space between the top of the valence band and the bottom of the conduction band. Depending on the substance, it could be big, tiny, or zero [1].

These different situations are depicted in Figure 1.3 and discussed below:

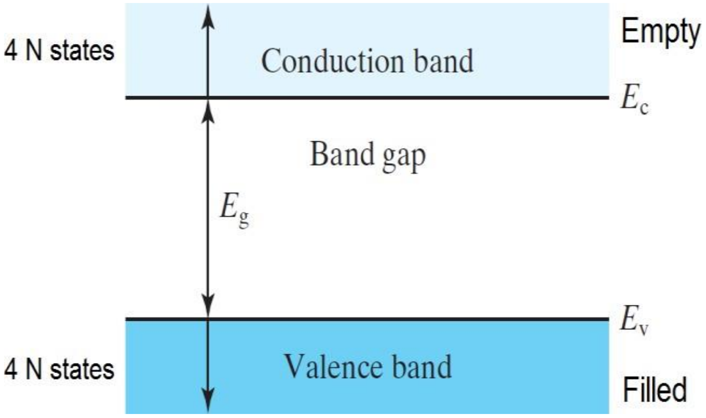

Figure 1.3: Energy levels of a semiconductor

1.2.1. Insulators:

Figure 1.4(a) shows that there is a substantial energy band gap (Eg > 3 eV). There are no electrons in the conduction band, so electrical conduction is not possible. When it comes to insulators, the energy gap is so great that thermal excitation is unable to drive electrons from the valence band to the conduction band [1].

1.2.2. Semiconductors:

As shown in Figure 1.4(b), there is a small but limited energy band gap (Eg < 3 eV). Because of the small band gap, some electrons from the valence band can gain enough energy to cross the energy gap and reach the conduction band at ambient temperature. Despite their small quantity, these electrons have conduction band mobility [1].

1.2.3. Conductors:

As seen in Figure 1.4(c), the conduction band is partially filled and the balanced band is partially vacant, or the conduction and the valence bands overlap. Electrons from the valence band can readily migrate into the conduction band when there is overlap. This releases a significant amount of electrons for electrical conduction. Conduction is made possible when the valence band is partially empty because electrons can go from its lower level to its higher level [1].

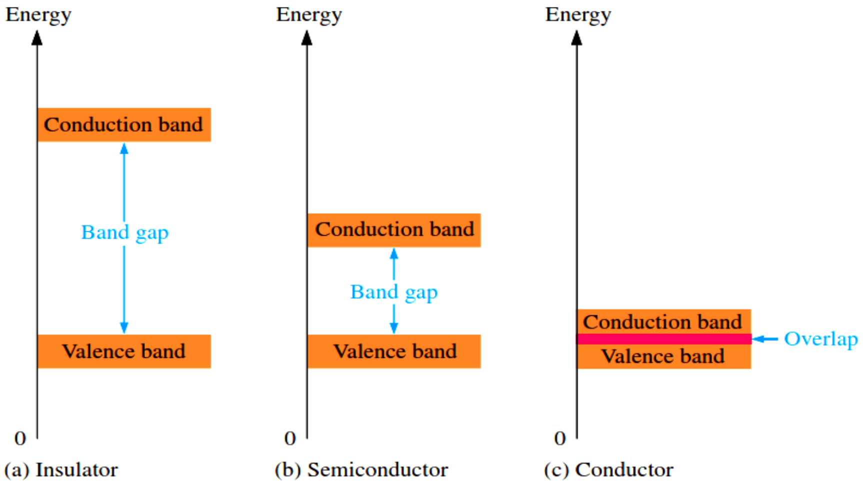

Figure 1.4: Difference between energy bands of (a) insulators, (b) semiconductors, and (c) conductors.

1.3. Semiconductors:

1.3.1. The Fermi-Dirac distribution function and Fermi level:

A semiconductor's conduction band is made up of a large number of accessible, permitted, and unoccupied energy levels.

Two considerations are taken into account when determining the number of electrons that will fill these levels, be tallied in n, and contribute to conductivity:

- Within a particular energy range, how many different energy levels are there?
- What is the probability that an electron will occupy each level?

The Fermi-Dirac distribution function is a probability function that provides the likelihood of the second item. The probability that an electron will fill a level with energy E is represented by the equation f(E), which is as follows: $f(E) = \frac{1}{1+\exp\left((E-E_f)/(k_B T)\right)}$ (1.1)

(1-f(E)) is the likelihood that the energy level E will be empty (have a hole), since f(E) is the probability that an electron will fill it.

f(E) near EF, it is readily demonstrated that

$$f\left(E_f + E\right) = 1 - f\left(E_f - E\right) \qquad (1.2)$$

1.3.2. Intrinsic semiconductors:

An intrinsic semiconductor is a pure undoped semiconductor, i.e., there is no foreign atom in its crystal lattice and no mobile carriers at 0° K. When an electron in an intrinsic semiconductor gets enough energy (T > 0° K), it can go to the conduction band and leave behind a hole. This process is called electron-hole pair creation.

1.3.2.1. Carrier concentration:

Since electrons and holes are always formed in pairs for the intrinsic material, ni represents the intrinsic carrier concentration.

$$n = p = n_i \qquad (1.3)$$

1.3.2.2. Fermi level:

In an intrinsic semiconductor, n=p. It indicates that there is an equal probability of finding an electron at the conduction band edge as there is of finding a hole at the valence band edge if we apply the band-symmetry approximation, which postulates that there are equal numbers of states in equal-sized energy bands at the edges of the conduction and valence bands:

$$f(E_c) = 1 - f(E_v) \qquad (1.4)$$

We can deduce from Eq. 1.4 that for an intrinsic semiconductor, the Fermi level EF needs to be in the middle of the bandgap. This level is actually referred to as the "intrinsic Fermi level," as demonstrated by EFi:

$$E_{Fi} = E_c - \frac{E_g}{2} = E_v + \frac{E_g}{2} \qquad (1.5)$$

where Eg is the bandgap energy.

1.3.3. Extrinsic semiconductors:

By including impurities, also known as dopant atoms, to increase the intrinsic semiconductor's carrier concentration and hence its electrical conductivity, the intrinsic semiconductor can be changed into an extrinsic semiconductor.

a- n-type:

Only four electrons are used to form covalent bonds with neighboring atoms when one of the atoms in the semiconductor crystal is replaced by a pentavalent donor atom (such as phosphorus (P), arsenic (As), or antimony (Sb). The fifth electron is free to jump to the conduction band at room temperature, leaving a positively charged atom behind. This extra electron can be used for conduction. The donor atoms' ionization or activation are other names for this process.[3]

After ionization, the positively charged donor atom that remains is stationary and has no role in conduction. The electron that is ionized and leaves the atom is measured by the electron concentration, or n. Since there is little activation energy, nearly all of the conduction band will receive an electron from the donor atoms present in the crystal. This means that for an n-type material at equilibrium, where ND is the donor concentration:

$$n_0 \approx N_D [cm^{-3}] \qquad (1.6)$$

b- p-type:

In this case, the dopant atoms are acceptor atoms. Boron (B), aluminum (Al), and gallium (Ga) can all be used as acceptors for silicon. These elements, which have three electrons in their outermost shell, belong to column III. One of the acceptor atoms' valence shells can easily take in an electron from the silicon valence band when these atoms are present in the silicon crystal, leaving a hole that makes the acceptor atom negatively charged.

After an electron joins its valence shell, the negatively charged acceptor atom is stationary and does not contribute to conduction. That electron leaves a hole, which is measured in the hole concentration, p. Since there is low activation energy, nearly all of the electrons from the valence band will be taken by the acceptor atoms present in the crystal. Given a p-type material in equilibrium and an acceptor concentration of NA, we can calculate:

$$p_0 \approx N_A[cm^{-3}] \qquad (1.7)$$

Both types, n-type and p-type, of extrinsic semiconductors can be explained by the illustrated structure in Figure 1.5:

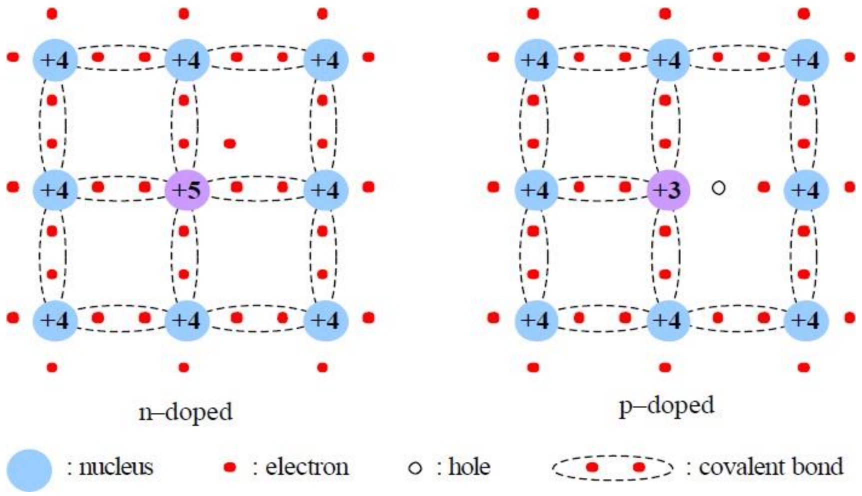

Figure 1.5: Structure of extrinsic semiconductors, n-doped and p-doped.

1.3.3.1. Carrier concentration:

If (n) is greater than (p) and the concentration of donor atoms (ND) is greater than the concentration of acceptor atoms (NA), the semiconductor material is n-type:

$$n = N_D - N_A \quad Where \quad p = \frac{n_i^2}{n} \qquad (1.8)$$

If NA is greater than ND, then the semiconductor material is p-type, since p is greater than n.

$$p = N_A - N_D \quad Where \quad n = \frac{n_i^2}{p} \qquad (1.9)$$

We must investigate what is meant by the electron and hole densities in the valence and conduction bands, respectively, in order to understand the behavior of semiconductors. The number of states (per unit volume and per unit energy) between E and E+dE is indicated by the parameter N(E): The physical "room" available for electrons (or holes) in the conduction band (or valence band) is represented by Nc(E) (or Nv(E)). In energies close to the extremes of these two bands, the density of states depends quadratically on E:

$$N_c(E) = \frac{1}{2\pi^2}\left(\frac{2m_c}{h^2}\right)^{3/2} \sqrt{E - E_c} \; cm^{-3}/eV \qquad (1.10)$$

$$N_v(E) = \frac{1}{2\pi^2}\left(\frac{2m_c}{h^2}\right)^{3/2} \sqrt{E_v - E_c} \; cm^{-3}/eV \qquad (1.11)$$

Where mc (resp. mv) is the average effective mass of the conduction band (resp. of the valence band) and =h/2π is the normalized Planck constant. The effective mass of an electron me (resp. a hole mh) in a direct gap semiconductor is represented by mc (resp. mv). The density of states isn't the only information we need to determine how many electrons and holes are present in each band. In addition, we need to determine the likelihood that an electron with a particular energy E will occupy a level. The Fermi-Dirac distribution function provides this probability:

$$f(E) = \frac{1}{1 + \exp\left((E - E_f)/(k_B T)\right)} \qquad (1.12)$$

1-f(E) yields The likelihood that a hole will occupy an energy level E since a hole is defined as the absence of an electron. The number of states that may be occupied by electrons of energy E, weighted by the probability to "find" an electron having this specific energy, is integrated over the range of energies accessible by electrons in the band to obtain the electron density n [cm-3] (or, alternatively, the hole density p) in the conduction band (valance band):

$$n = \int_{E_c}^{+\infty} N_c(E) f(E) dE \qquad (1.13)$$

$$p = \int_{-\infty}^{Ev} N_v(E)\big(1 - f(E)\big) dE \qquad (1.14)$$

There are a lot of free holes in a p-type semiconductor at thermal equilibrium, or, to put it another way, (p) is approximately equivalent to the density of doped acceptor impurities, which gives rise to the p-type conductivity. Given is the hole concentration (p).

$$p = N_v \exp\left(\frac{E_v - E_f}{kT}\right) \qquad (1.15)$$

EF moves towards EV as acceptor density rises. Furthermore, the concentration of the extremely tiny amount of unbound electrons is provided by:

$$n = N_c \exp\left(-\frac{E_c - E_f}{kT}\right) \qquad (1.16)$$

Given that (EC–EV) is the semiconductor's intrinsic forbidden band gap Eg, the product p.n is independent of the type and density of impurities. As a result, the product's square root, known as intrinsic concentration, is defined as:

$$n_i = \sqrt{np} = \sqrt{N_c N_v} \exp\left(-\frac{E_g}{2kT}\right) \qquad (1.17)$$

1.3.3.2. Fermi level:

The conduction band of an n-type semiconductor has more electrons than holes compared to the valence band. This suggests that there is a higher chance of discovering an electron close to the conduction band edge than there is of finding a hole at the valence band edge. The Fermi level is therefore closer to the conduction band in an n-type semiconductor:

n – type: $f(E_c) > \big(1 - f(E_v)\big) \quad E_F > E_{Fi} \qquad (1.18)$

In the valence band of a p-type semiconductor, there are more holes than electrons in the conduction band. This suggests that the likelihood of discovering an electron close to the conduction band boundary is lower than the likelihood of discovering a hole at the valence band boundary. The Fermi level is therefore closer to the valence band in an n-type semiconductor. These final points are summed up by the relationships listed below:

p – type: $f(E_c) < \left(1 - f(E_v)\right) \quad E_F < E_{Fi}$ (1.19)

1.4. Studied semiconductors:

1.4.1. CdS:

CdS is an II-VI group semiconductor having a bandgap 2.45 eV. For a long period of time, researchers have attracted towards the CdS thin film due to its interesting optoelectronic properties. It is widely used as a buffer layer in solar cells because of its superior optoelectronic properties.

The optical transparency of the film can be easily controlled by thickness variation. Another interesting property of this material is it provides chemical and thermal stability to the Cigs thin film.[4]

1.4.2. CIGS:

The characteristics of the absorber material have a major impact on the efficiency of a CIGS-based solar cell. Similar to other semiconductors, CIGS's optical and electrical characteristics can be significantly influenced by its composition and crystalline structure. Thus, to optimize a CIGS-based device, a thorough understanding of this material's structure is required [5].

1.4.2.1. Crystal Structure:

The fundamental component of CIGS is CIS (CuInSe2). It is a semiconductor with a chalcopyrite crystalline structure, classified as I-III-VI2. This tetragonal structure can be thought of as the stacking of two zincblende structures, where atoms from groups III (Se) (anions) occupy the tetrahedral sites and atoms from groups I (Cu) and II (In) (cations) occupy the other sites in an orderly fashion. Tetrahedral distortion, or the minor deviation of the lattice parameter ratio c/a from 2 caused by the energy differences between the Cu-Se and In-Se bonds, is explained [6].

In the case of CIGS, In or Ga atoms, in varying amounts depending on the alloy composition, occupy the positions of the group III atoms. CIGS, on the other hand, is a solid combination of CuInSe2 and CuGaSe2. The crystalline structures of the three semiconductor materials used in photovoltaics—Si, CdTe, and CIGS—are shown differently in Figure 1.8.

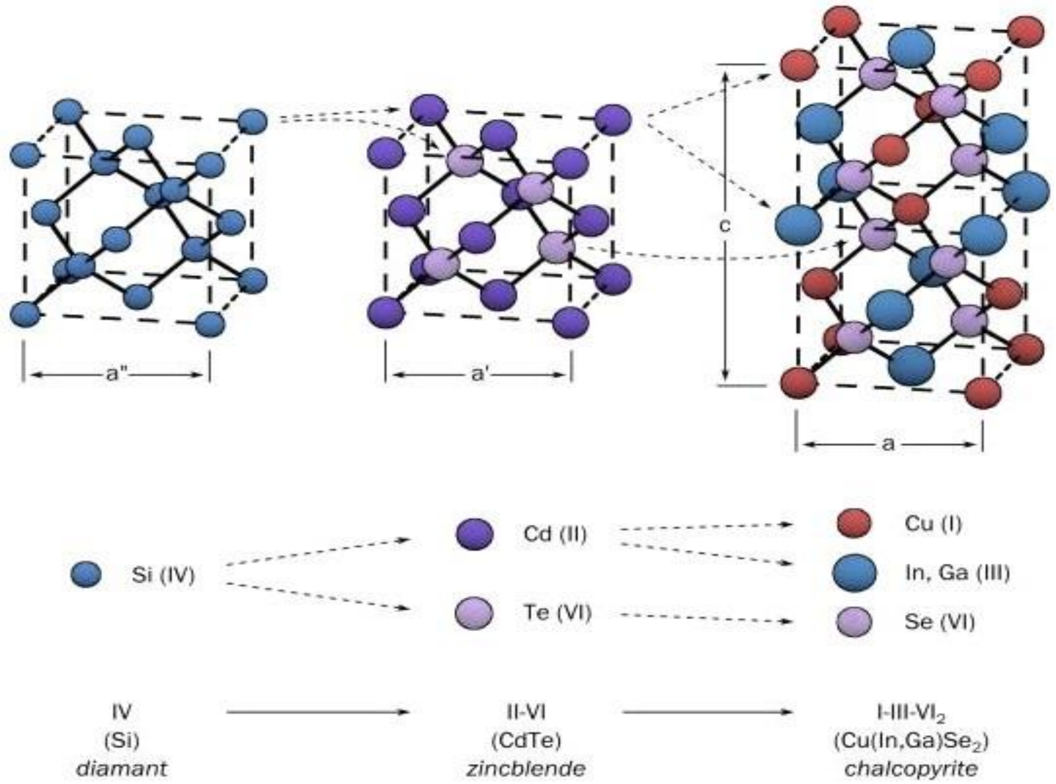

Figure 1.6: Comparison of unit cells of crystal structures of Si, CdTe and CIGS

1.4.2.2. Electronic Properties:

a. Band Structure:

Semiconductor materials CuInSe2 and CuGaSe2 have direct band gaps of 1.68 eV and 1.035 eV, respectively. This discrepancy is primarily due to a variation in the conduction band minimum (EC). CIGS is a solid combination of these two compounds, as was previously stated.

The fraction of gallium atoms replacing indium atoms in the structure is given by the ratio x = Ga/(In+Ga). According to the following empirical law, the band gap width of CIGS varies with x between pure CIS and pure CGS:

$$E_g = 1.035 + 0.65x - 0.264x(1 - x) \qquad (1.20)$$

As a result, depending on the gallium content, the Eg of CIGS can be varied between 1.035 eV and 1.68 eV. Several variables determine the ideal value of Eg. A lower value of Eg is better from the standpoint of photon absorption since it permits the absorption of a larger spectrum (longer wavelengths). As a result, the solar cell delivers a higher current (Jsc). Nonetheless, the maximum voltage that the cell can deliver is determined by the value of Eg. In order to optimize conversion efficiency, the perfect balance between voltage and current must be reached. According to the majority of experimental findings in the field of CIGS cells, the optimal efficiencies are reached at a gap of roughly 1.2 eV, or a gallium concentration of almost 30% [7].

The energy of the band gap is related to the wavelength of the photon by:

$$E_g(eV) = \frac{1.24}{\lambda(\mu m)} \qquad (1.21)$$

Where λ is the light wavelength in micrometers and Eg is the band gap energy in electron volts [8].

b. Doping:

The CIGS used in standard cells is of the p-type. This doping results from intrinsic doping, which is caused by crystalline flaws that create acceptor states. These values for CIGS vary slightly depending on the gallium content.

The acceptor levels are primarily caused by indium vacancies (VIn) and copper vacancies (VCu), as well as copper substitutions for indium (CuIn). Nonetheless, there are two primary reasons why VCu and p-type doping in CIGS are connected. First, they provide an acceptor level that is quite near the valence band maximum (0.03 eV). Secondly, they have the most favorable formation energy (Ef = 0.6 eV). The defect-generating donor levels (InCu and Cu_i) have a significantly higher formation energy than VCu. Consequently, the p-type doping of CIGS is caused by the latter defect's abundance.

1.4.2.3. Optical properties of CIGS:

The direct band gap of CIGS makes it suitable for use in thin-film solar cells. Consequently, photons with energies around the gap can be absorbed without the need for phonon intervention, leading to a high optical absorption coefficient α (in contrast to a semiconductor like silicon that has an indirect band gap). The absorption coefficient for a given photon energy hv is approximately given by [9]:

$$\alpha(hv) = A(hv - E_g)^{1/2} \qquad (1.22)$$

This connection demonstrates rather clearly how the band gap affects the range of energies that CIGS can absorb.

The optical absorption coefficients of Si and CIS, which represent the highest absorption range and the lowest gap for CIGS, respectively, are compared as a function of incident photon energy in Figure 1.4. The observation of an order-of magnitude difference between Si and CIS emphasizes the superiority of the latter in thin-film applications. Therefore, for photons with energy larger than Eg, a 1 μm thick layer of CIGS is adequate to absorb 95% of the solar spectrum.

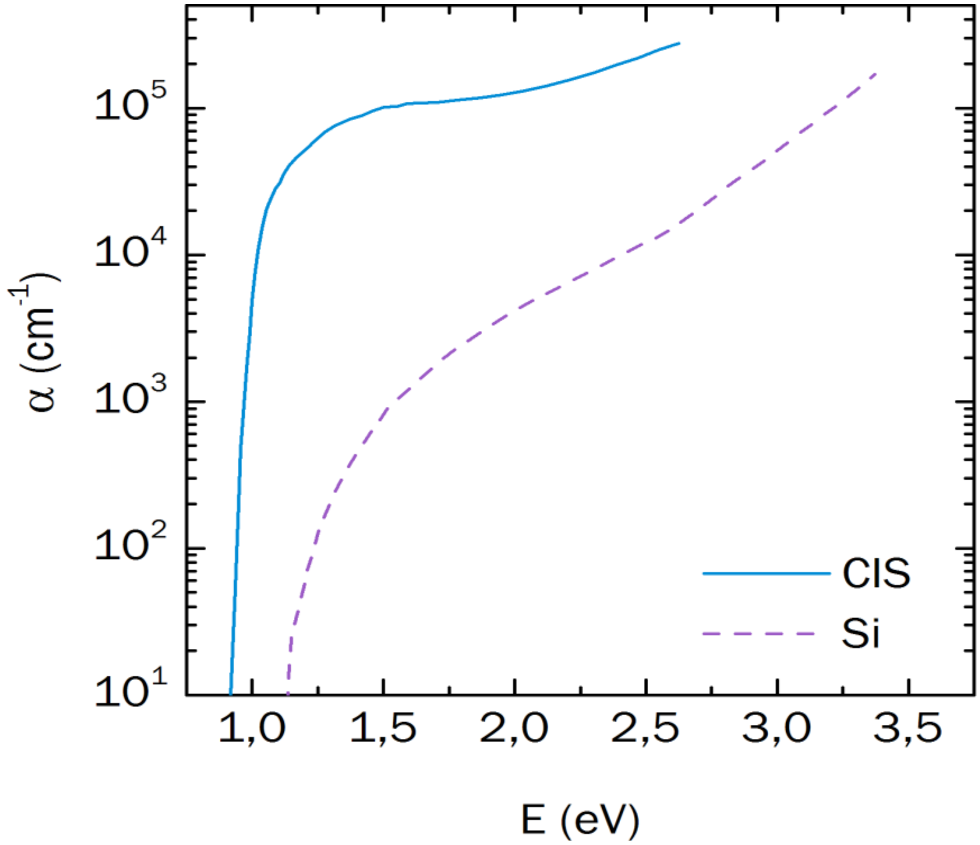

Figure 1.7: Optical absorption coefficient α as a function of energy ET of incident photons in CIS and Si

Optical Constant (Refractive Index):

The complex refractive index, η = n + ik (n: real index), is represented by the curves in Figure (1.5) for samples with x = 0 and 0.2 (x denoting the concentration of Ga in CIGS). Other optical metrics, such as the absorption coefficient, can be computed using the complex refractive index (k)[5]:

$$\alpha = \frac{4\pi k}{\lambda} \qquad (1.23)$$

Using k as the imaginary index and λ as the photon's wavelength[5].

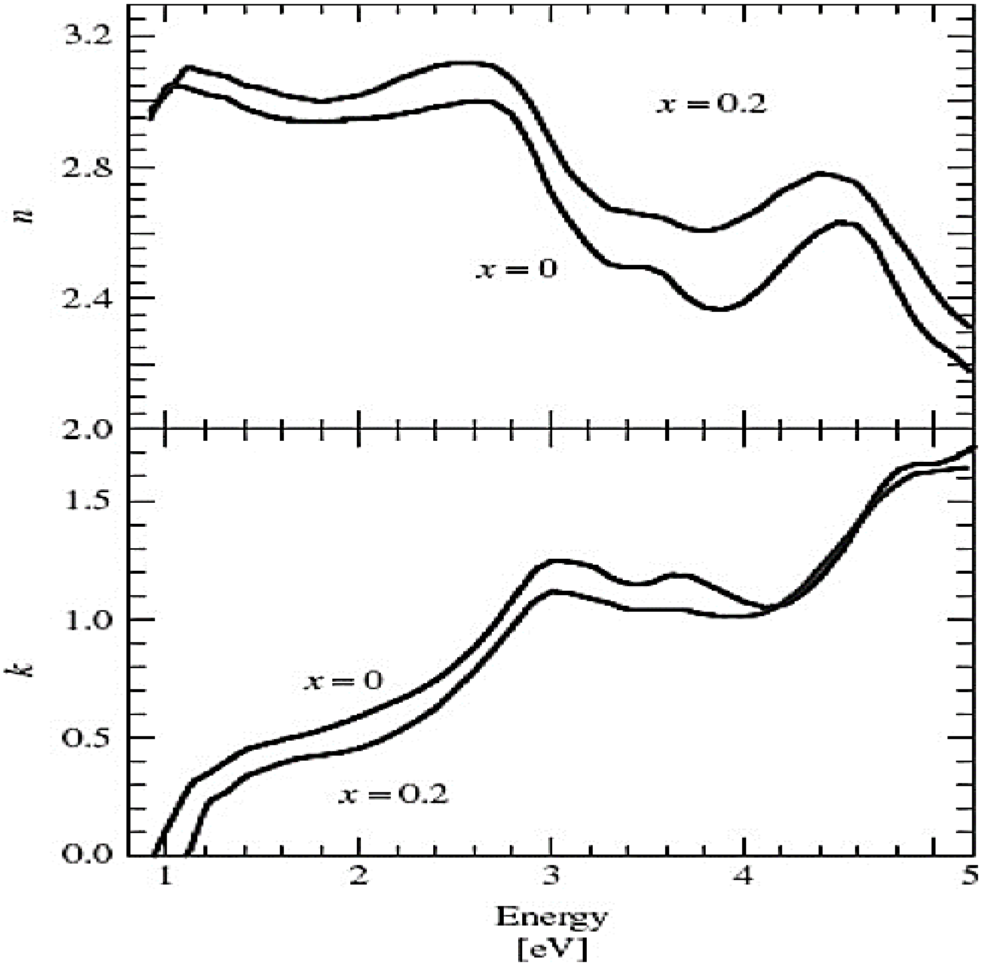

Figure 1.8: Representation of refractive indices (real and imaginary) as a function of energy for CIGS, with x=0 and x=0.2

1.4.3. CZTS:

The characteristics of the absorber material have a major impact on the efficiency of a CZTS-based solar cell. Similar to other semiconductors, CZTS's optical and electrical characteristics can be significantly influenced by its composition and crystalline structure. Thus, to optimize a CZTS-based device, a thorough understanding of this material's structure is required [10].

1.4.3.1. Crystal Structure:

The fundamental component of CZTS is Cu2ZnSnS4. It is a semiconductor with a kieserite crystalline structure, classified as I2-II-IV-VI4. This tetragonal structure can be seen as derived from the chalcopyrite structure, where atoms from groups II (Zn) and IV (Sn) substitute for group III atoms in the chalcopyrite CuInSe2 structure. The tetrahedral coordination of cations (Cu, Zn, Sn) with anions (S) exhibits slight distortions due to differences in bond lengths, influencing the material's electronic properties [11].

In CZTS, Zn and Sn atoms occupy the group II and group IV positions, respectively, in a structured manner. The crystal structure of CZTS is shown alongside those of other semiconductor materials used in photovoltaics—Si, CdTe, and CZTS—in Figure 1.9 [11].

The crystalline structures of the semiconductor material used in photovoltaics CZTS is shown in Figure 1.9.

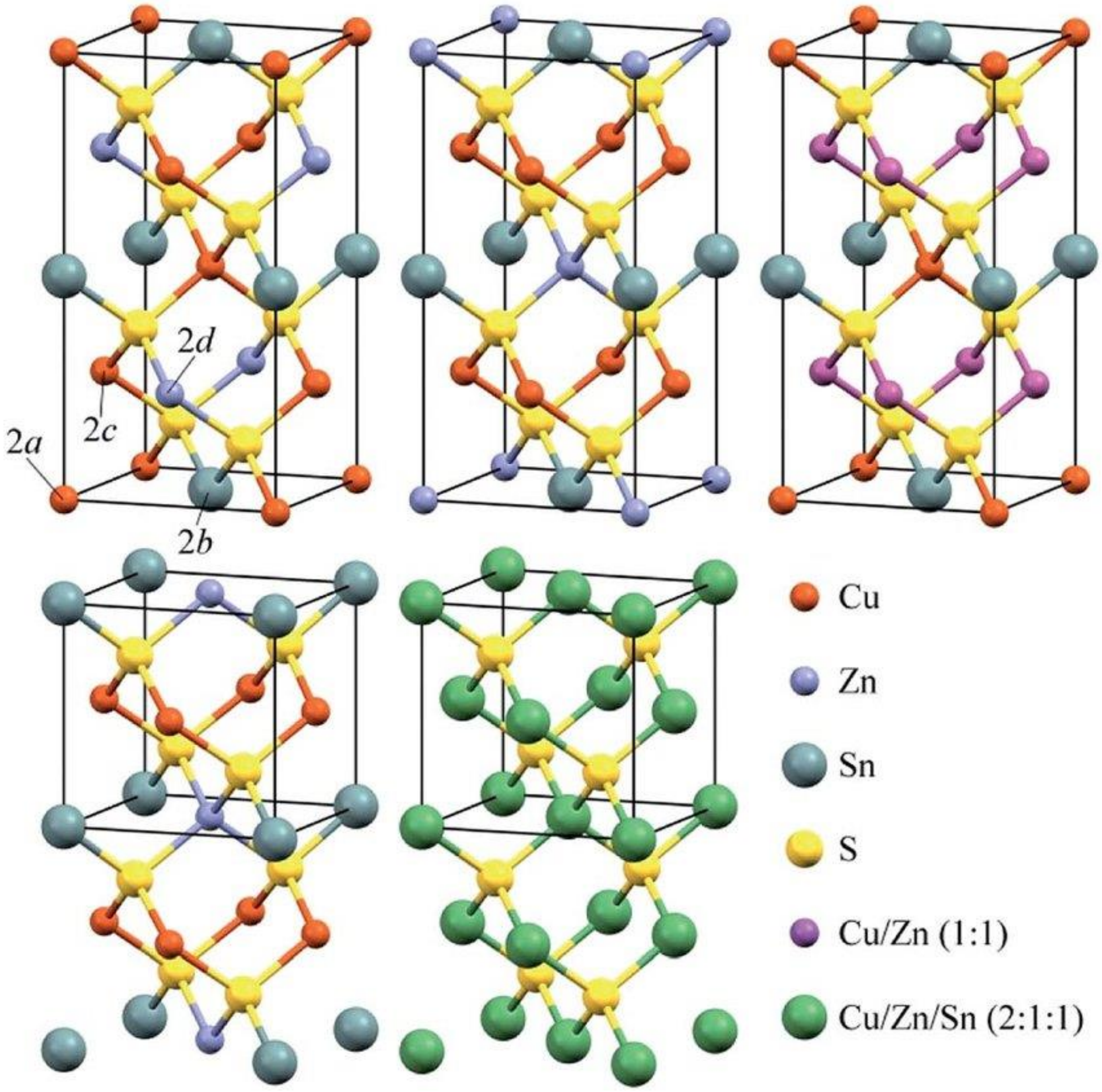

Figure 1.9: Unit Cells of Crystal Structures of CZTS

1.4.3.2. Electronic Properties:

a. Band Structure:

CZTS has a direct band gap of approximately 1.5 eV, suitable for solar energy absorption. The band structure is influenced by the composition, particularly the Zn/Sn ratio. The ideal band gap for CZTS-based solar cells balances photon absorption and the voltage generated by the cell. The band gap energy (Eg) of CZTS is well-suited for efficient solar energy conversion, allowing the absorption of a significant portion of the solar spectrum and generating a higher current (Jsc).

The empirical relationship between the band gap energy and the wavelength of absorbed light is given by:

$$E_g = \frac{h_c}{\lambda} \qquad (1.24)$$

where λ is the light wavelength in micrometers and E_g is the band gap energy in electron volts [12].

b. Doping:

The CZTS used in standard cells is typically p-type due to intrinsic defects in the crystal structure, such as copper vacancies (VCu) and zinc on copper antisites (ZnCu), which act as acceptor levels. These defects create shallow acceptor states near the valence band, facilitating p-type conductivity. The acceptor levels are primarily caused by copper vacancies and zinc substitutions, contributing to p-type doping [13].

1.4.3.3. Optical Properties of CZTS:

The direct band gap of CZTS makes it suitable for use in thin-film solar cells. Photons with energies close to the band gap can be absorbed efficiently without the need for phonon assistance, resulting in a high optical absorption coefficient (α). This high absorption coefficient is beneficial for thin-film applications as it allows a thin layer of CZTS to absorb most of the incident solar radiation.

The absorption coefficient for a given photon energy (hv) is approximately given by:

$$\alpha(hv) = A(hv - E_g)^{1/2} \qquad (1.25)$$

This relationship indicates how the band gap influences the range of energies that CZTS can absorb. Compared to silicon, CZTS has a higher absorption coefficient, making it more efficient in thin-film configurations [14].

For photons with energy greater than E_g, a 1 µm thick layer of CZTS is sufficient to absorb most of the solar spectrum, highlighting its efficiency as an absorber material in photovoltaic applications[14]

CHAPTER 2

SOLAR CELLS

2.1. Introduction:

There are two crucial phases in the photovoltaic energy conversion process in solar cells. First, an electron-hole pair is created when light is absorbed. The device's structure then divides the electron and hole, sending the electrons to the negative terminal and the holes to the positive terminal. thus producing electricity, as seen in Figure 2.1 [5].

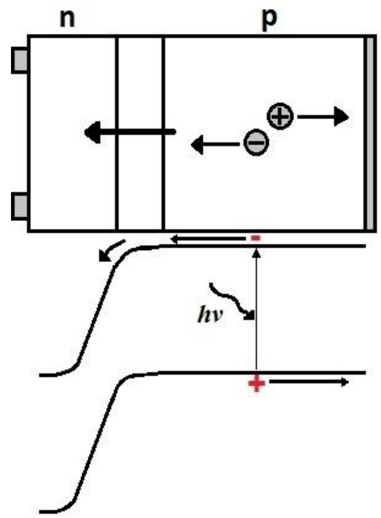

Figure 2.1: The bulk of the cell is formed by a thick p-type base where most of the incident light is absorbed and most power is generated.

2.2. Typical solar cell structures:

2.2.1. The p-n junction:

A fundamental grasp of the PN junction diode, including the electrical connections made to the diode, is necessary to comprehend all photovoltaic devices. Initially, current flow in one direction and current blocking in the other were provided by the semiconductor diode. As seen in Figure 2.2, PN connections are created by combining n-type and p-type semiconductor materials. Electrons diffuse from the n-type side to the p-type side because the n-type region has a high electron concentration and the p-type one has a high hole concentration. Holes flow in the opposite direction. When electrons and holes depart from a PN junction, they leave behind exposed fixed charges on the sites of dopant atoms. Between the n-type and p-type materials, an electric field E develops, creating a "built in" potential Vbi. Since the electric field sweeps free carriers away quickly, a "depletion region" is created [15].

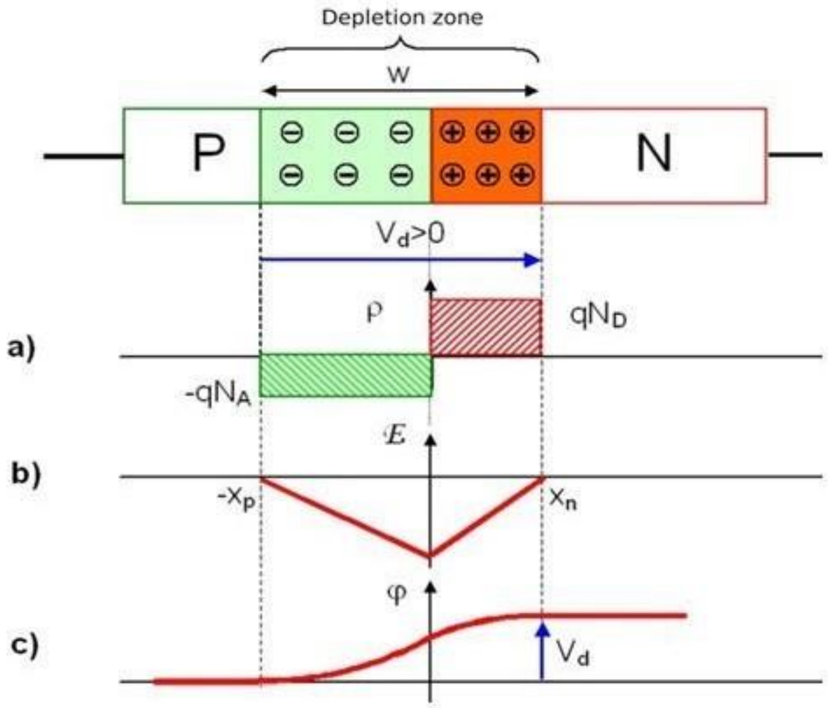

Figure 2.2: Formation of a PN junction in the Schottky approximation. (a) space-charge distribution due to fixed ionized dopants; (b) electric field obtained by integration of the Poisson equation; (c) a second integration step results in the electrostatic potential.

Certain carriers still diffuse over the connection despite the electric field creating a barrier. A few carriers will move quickly enough and in a net enough direction to pass through the intersection. When a majority carrier passes through the intersection, it turns becoming a minority provider. Before it recombines and creates the "diffusion current," it will continue to diffuse away from the junction and can traverse an average distance equal to the diffusion length. On the other hand, the "drift current" is the electric field in the depletion area that sweeps minority carriers that reach the edge of the diffusion region across it. The net current from the PN junction is zero in equilibrium as a result [15].

2.2.2. The p-n junction solar cell:

Since realistic approximations exist that enable the development and successful application of analytical solutions for the description of practical devices, the planar p-n junction solar cell under low injection is typically singled out for special examination. The fact that the cell can be clearly separated into three regions—the emitter, junction region, and base—each of which has a distinct function in the operation of a solar cell, is largely responsible for the model's effectiveness. The majority of the incident light is absorbed by the emitter and base, which are essentially neutral during cell operation, and they then move the photogenerated minority carriers to the junction. The minority carriers that are gathered from the emitter and base are separated by the p-n junction, which has a fixed space charge and a high electric field. The junction, also known as the depletion area, is essentially devoid of mobile charge carriers [5].

With the corresponding potentials $\phi n = q \times E_{Fn}$, and $\phi p = q \times E_{Fp}$, the Fermi level EF separates into two quasi-Fermi levels, EF and EFp, one for the electrons and one for the holes, during operation. As seen in Figure 2.3, the quasi-Fermi levels in the junction are parallel to the open circuit, have negligible gradients, and their splitting is equal to the observed voltage at the junction.

The electrostatic potential difference ΔΨ between the two sides of the junction under illumination or under applied bias in the dark is the difference of two terms: the voltage V at the junction edges and the equilibrium built-in voltage Vbi [5]:

$$\Delta\Psi = V_{bi} - V \qquad (2.1)$$

$$qV_{bi} = k_B T ln \frac{N_D N_A}{n_i^2} \qquad (2.2)$$

Where the concentrations of donors and acceptors on the p and n sides of the junction, respectively, are denoted by the letters NA and ND. V is the same as the voltage recorded at the cell's terminals when resistive losses are not present. The formula for the junction width Wj is provided by [5].

$$W_j = L_D \sqrt{\frac{2q\Delta\Psi}{k_B T}} \qquad (2.3)$$

Here, LD is the Debye length [5],

$$L_D = \sqrt{\frac{\varepsilon k_B T}{q^2 N_B}} \qquad (2.4)$$

where ε is the static dielectric constant.

The junction, also known as the depletion zone, functions as a lossless mechanism in an ideal p-n junction solar cell to harvest and separate the minority carriers from the quasi-neutral areas, which are the emitter and base. Afterwards, the junction's functionality can be summed up as border conditions that connect the concentrations of minority carriers on one side of the junction and majority carriers on the other [5].

The photogenerated and dark saturation currents for the cell are obtained by adding the relevant quantities for the base and the emitter:

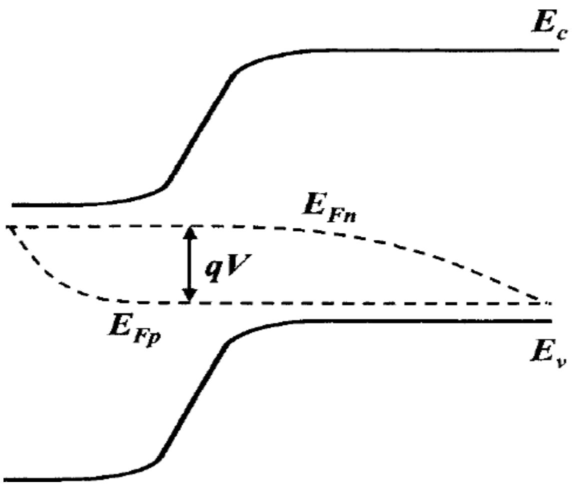

Figure 2.3: The p-n junction at open circuit.

$$I_{ph} = I_{ph} + I_{phe} \quad and \quad I_0 = I_{0b} + I_{0e} \qquad (2.5)$$

An ideal p-n junction has no recombination, but the (little) light-generated current created here can be added to the first equation (2.5). More realistic analytical theories contain recombination. The Shockley-Read-Hall model of recombination is used in the original treatment. via flaws, primarily resulting in a present reduction of a phrase of the kind $I_{02}(\exp(qV/2\,k_B T) - 1)$ [5]

2.2.3. Homojunction and Heterojunction:

Heterojunction and Homojunction are two different categories for junctions made of two semiconductor materials. Homojunction refers to PN junctions made of identical semiconductors. Two distinct semiconducting materials with uneven band gaps combine to generate the latter. How a semiconductor behaves alignment of the energy bands at the interface is critical to the connection [5]. As seen in Figure 2.4, semiconductor interfaces can be categorized into three different forms of heterojunctions [5], [16].

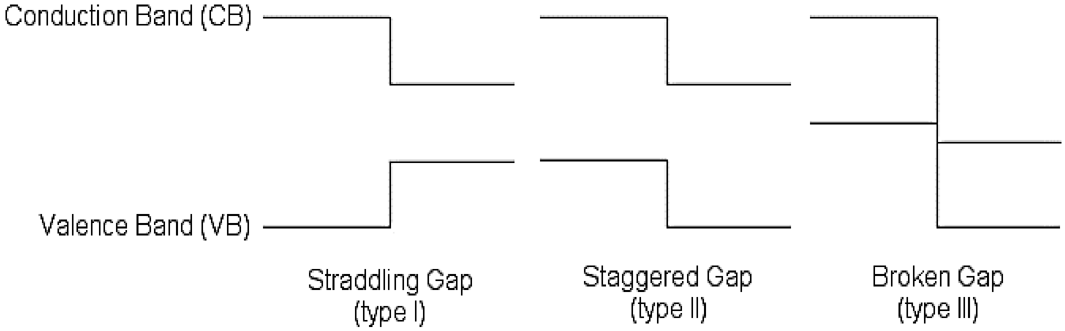

Figure 2.4: The three types of semiconductor Heterojunction organized by band alignment.

We apply the Anderson's electron affinity rule to build the energy band diagrams of a heteronucleon. The two semiconductors on either side of the heterojunction should have aligned (or at the same energy) vacuum levels.

After the alignment of the vacuum levels, it is It is possible to determine the conduction band and valence band offsets using the electron affinity and band gap values for each semiconductor. The energy differential between the semiconductor's vacuum level and the lower edge of the conduction band is provided by the electron affinity (χ). The energy difference between the upper edge of the valence band and the lower edge of the conduction band is shown by the band gap (Eg). To compute these values for semiconductor alloys, Vegard's law may be required (see Figure 2.5). [17], [18], and [16].

The valence band (ΔEV) and conduction band (ΔEC) band offsets can be computed using Anderson's rule. Poisson's equation can be used to determine the form of the band bending in the two semiconductors after using Anderson's rule to determine the bands' alignment at the junction [16]:

$$\Delta E_c = x_2 - x \qquad (2.6)$$

Let us now assume that semiconductor 2 has a sufficiently big band gap such that semiconductor 1's valence band is located at a higher energy than semiconductor 2's. The valence band offset is therefore provided by [16]:

$$\Delta E_y = (x + E) - (x_2 + E_2) \qquad (2.7)$$

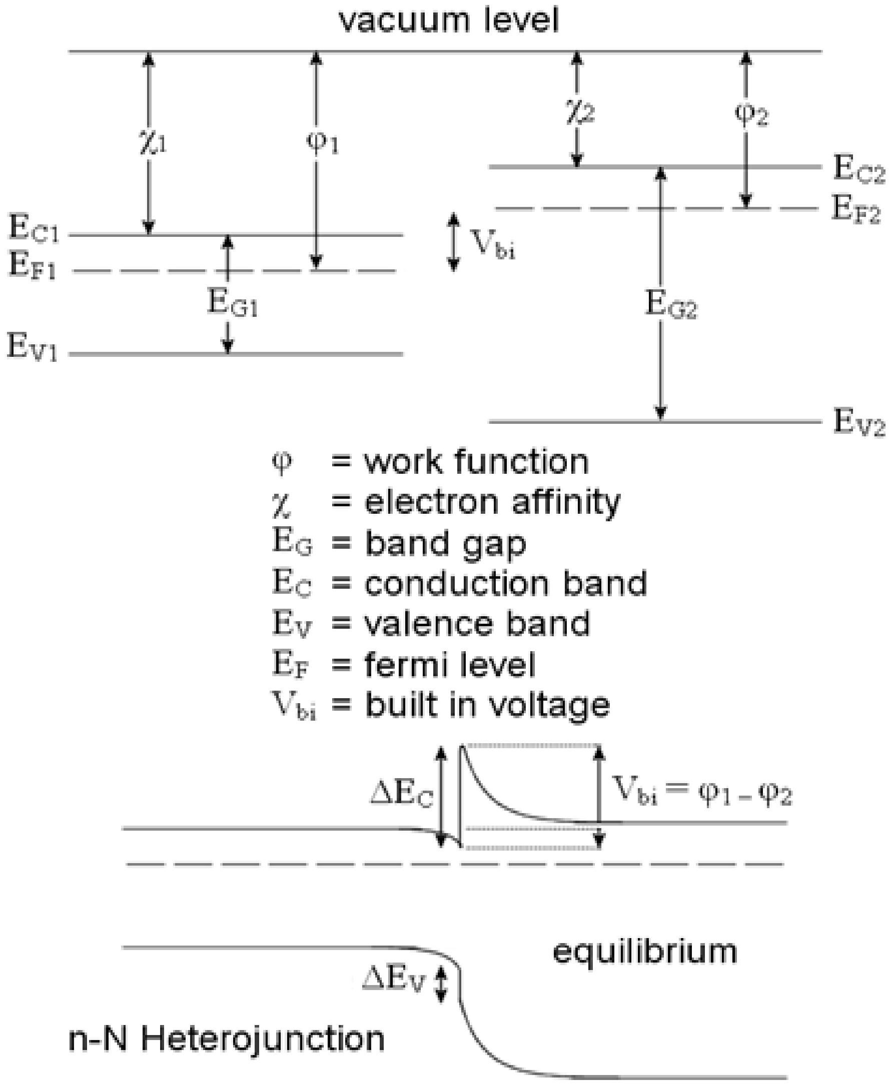

Figure 2.5: Band diagrams for straddling-gap Heterojunction.

2.3. Electrical characteristics:

2.3.1. The ideal solar cell:

An ideal solar cell can be represented by a current source connected in parallel with a rectifying diode, as shown in the equivalent circuit of Figure 2.6.

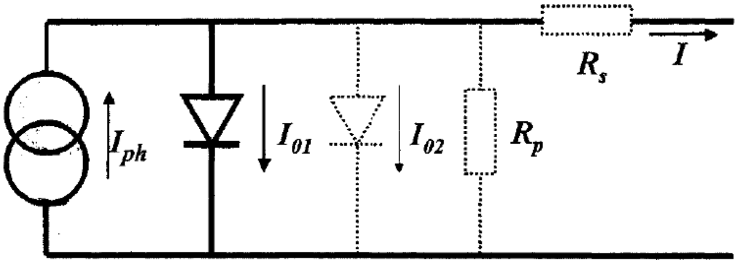

Figure 2.6: The equivalent circuit of an ideal solar cell (full lines). Non-ideal components are shown by the dotted line.

The corresponding I-V characteristic is described by the Shockley solar cell equation [17],

$$I = I_{ph} - I_0(e^{\frac{qV}{k_B T}} - 1) \qquad (2.8)$$

where kB is the Boltzmann constant, T is the absolute temperature, q (>0) is the electron charge,and V is the voltage at the terminals of the cell. I0 is well known to electronic device engineers as the diode saturation current.

In the ideal case, the short circuit current Isc is equal to the photogenerated current Iph, and the open circuit voltage Voc is given by [17]:

$$V_{oc} = \frac{k_B T}{q} \ln(1 + \frac{I_{ph}}{I_0}) \qquad (2.9)$$

The power P = IV produced by the cell is shown in Figure 2.8. The cell generates the maximum power Pmax at a voltage Vm and current Ira, and it is convenient to define the fill factor FF by[18]:

$$FF = \frac{I_m V_m}{I_{sc} V_{oc}} = \frac{P_{max}}{I_{sc} V_{oc}} \qquad (2.10)$$

The subscript 0 will provide the fill factor FF of a solar cell with the ideal characteristic Eq. (2.8). Though it can not be determined analytically, it can be demonstrated that FF0 is solely dependent on the ratio⁄. FF0 can be ascertained with remarkable precision using the approximative expression [17].

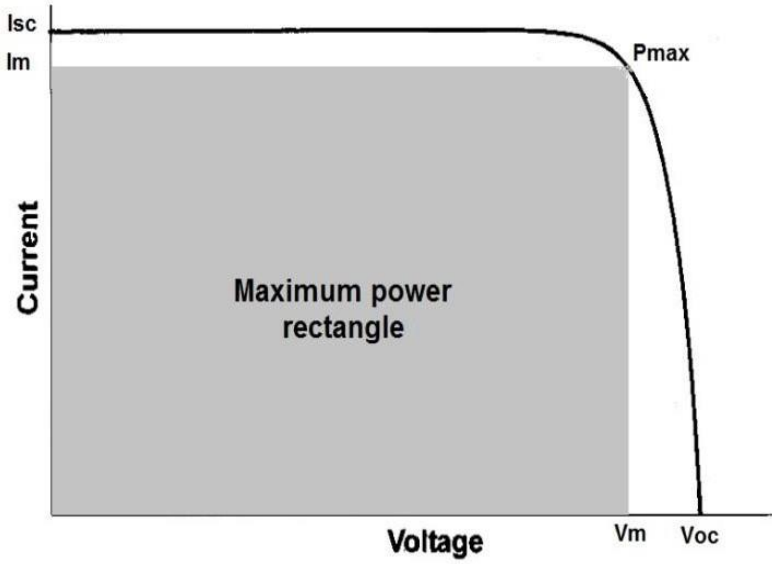

Figure 2.7: The I-V characteristics of a solar cell. The power generated at the maximum power point is equal to the shaded rectangle.

$$FF_0 = \frac{V_{oc} - \ln(V_{oc} + 0.72)}{V_{oc} + 1} \qquad (2.11)$$

The power generated at the maximum power point is equal to the blue rectangle in Figure 2.8.

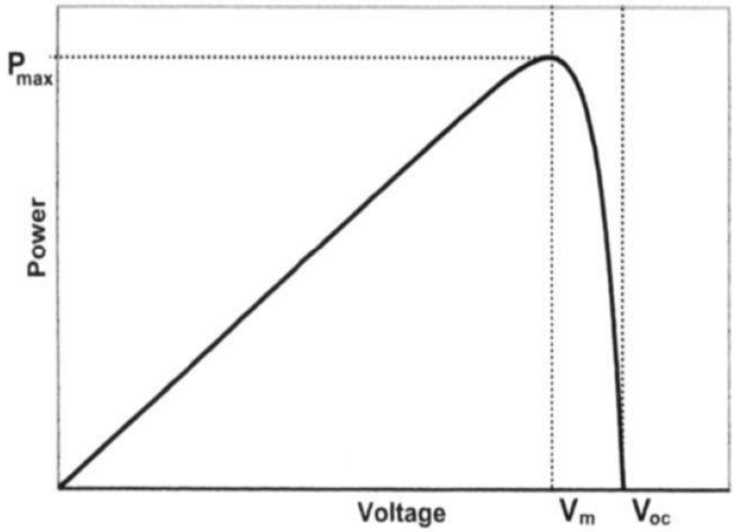

Figure 2.8: The power produced by solar cell.

The superposition principle is followed by the I-V characteristics of an ideal solar cell; the functional dependency, Eq. (2.8), can be derived from the analogous characteristic of a diode in the dark by shifting the diode characteristic down the current axis by Iph.

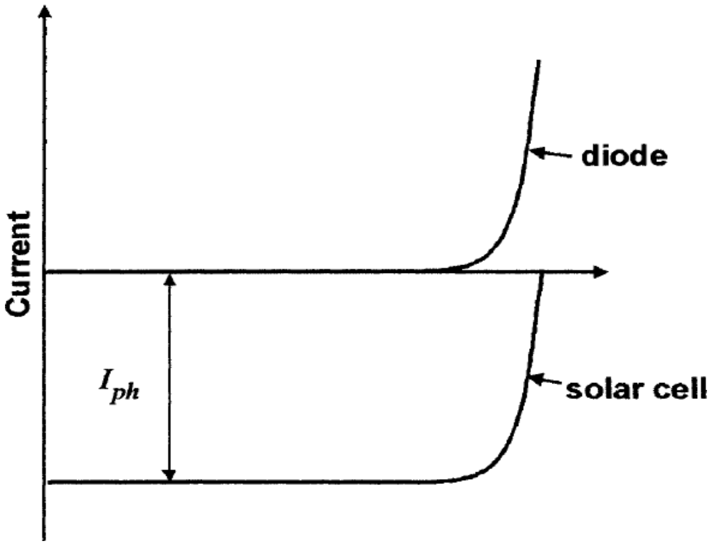

Figure 2.9: The superposition principle for solar cells.

2.3.2. Reel solar cell characteristics:

In real-world applications, a solar cell's I-V characteristic typically deviates slightly from the ideal characteristic equation (2.8). When fitting an observed curve, a two-diode model is frequently employed, where the second diode has an ideality factor of 2 in the denominator of the exponential term's argument.

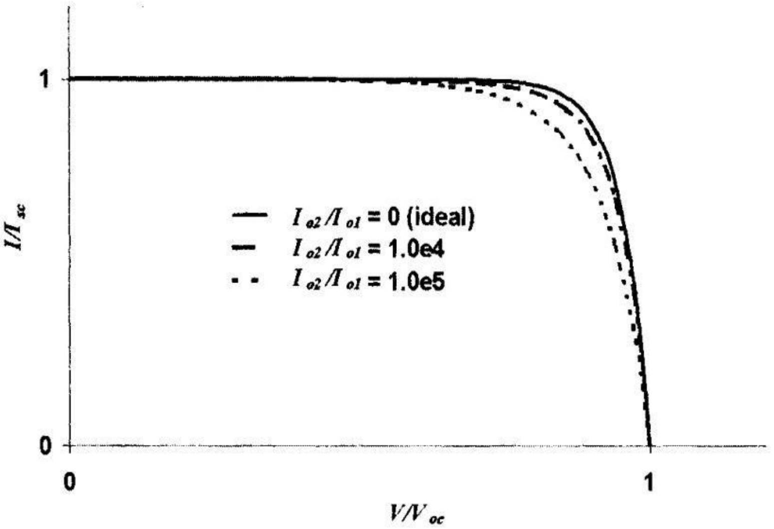

Figure 2.10: The I-V characteristic of the solar cell in the two diode model for three values of the ratio I02/I01.

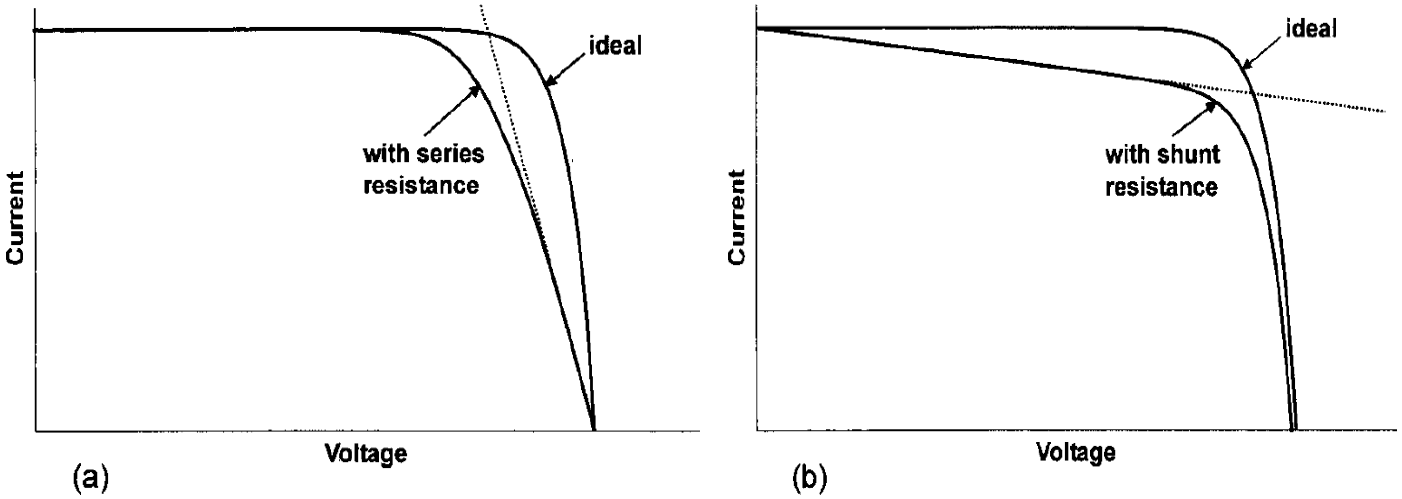

Figure 2.11: The effect of the series resistance (a) and parallel resistance (b) on the I-V characteristic of the solar cell.

The solar cell (or circuit) may also contain series (Rs) and parallel (or shunt, Rp) resistances, leading to a characteristic of the form [17],

$$I = I_{ph} - I_{01}\left[exp\left(\frac{V+IR_s}{k_BT}\right)-1\right] - I_{02}\left[exp\left(\frac{V+IR_s}{2k_BT}\right)-1\right] - \frac{V+IR_s}{R_p} \qquad (2.12)$$

where, as we've already mentioned, the light-generated current Iph may, in some cases, rely on the voltage. The dotted lines in Figure 2.6's equivalent circuit depict these properties. Figures 2.10 and 2.11, respectively, illustrate the impact of the second diode and the series and parallel resistances on the solar cell's I-V characteristic[17]. Writing will allow for the influence of the series resistance on the fill factor.

$$FF = FF_0(1-r_s) \qquad (2.13)$$

where$r_s = {}^{R_sI_{sc}}/_{V_{oc}}$. An equivalent expression exists also for the parallel resistance.

Further information about these parameters can be obtained from the dark characteristic (Figure 2.12).

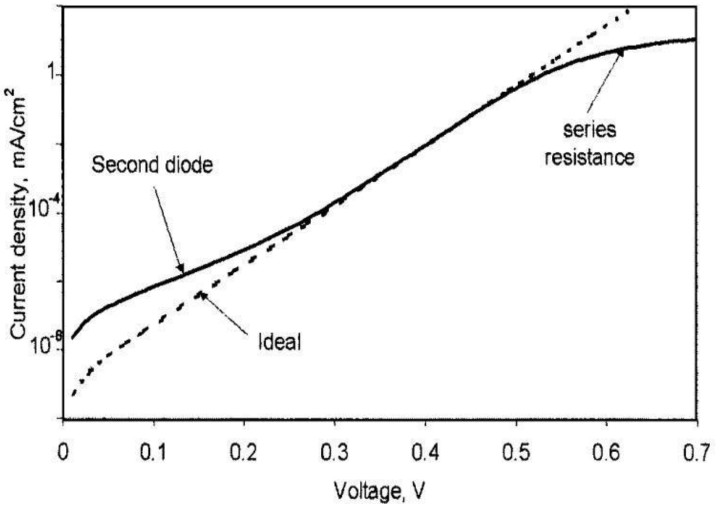

Figure 2.12: The dark I-V characteristic of a solar cell for the two-diode model including the series resistance. The shunt resistance has a similar effect to the second diode.

2.4. The quantum efficiency:

The ratio of the number of electrons in the external circuit created by an incident photon of a specific wavelength is known as the quantum efficiency of a solar cell. Consequently, it is possible to define external and internal quantum efficiencies (represented, respectively, by $EQE(\lambda)$ and $IQE(\lambda)$. Their approaches to handling photons reflected from the cell are different: only photons that are not reflected are taken into account in the value of IQE, but all photons impinging on the cell surface are included in the EQE value [17].

If the internal quantum efficiency is known, the total photogenerated current is given by:

$$I_{ph} = q\int_{(\lambda)} \Phi(\lambda)[1 - R(\lambda)]IQE(\lambda)\, d\lambda \qquad (2.14)$$

When $R(\lambda)$ is the reflection coefficient from the top surface, $\Phi(\lambda)$ is the photon flux impinge on the cell at wavelength l, and the integration is performed over all wavelengths l of light absorbed by the solar cell. Using interference filters or monochromators, the internal and external quantum efficiency values are frequently tested to evaluate a solar cell's performance.

2.5. Thin film solar cells:

2.5.1. The use of thin films in solar cells:

For almost 40 years, researchers have been studying thin film solar cells. Due to surface recombination effects and the difficulties of establishing a very shallow junction (less than 0.1 µm) with a high conductivity surface layer, all effective devices have a heterojunction configuration, in a heterojunction solar cell, the two semiconductors with opposite conductivity types are commonly referred to as the "absorber" (bandgap energy Eg1) and the "collector" or "window" (bandgap energy Eg2), respectively, with Eg2 > Eg1. The radiation strikes the window's surface, and photons with energy between Eg2 and Eg1 create hole-electron pairs inside the absorber. likewise reach the absorber, contingent upon the window's thickness and absorption coefficient.

The absorber is p-type because wide gap semiconductors for windows often have n-type conductivity. Electrons produced in the absorber's depletion area make up the majority of the photocurrent. According to how solar radiation impinges on the cell, heterojunction solar cells can be divided into frontwall and backwall types in practice [19].

In thin-film solar cells, a variety of binary and ternary compounds have been employed as absorbers and windows. Potential window materials include CdO, CdS, ZnO, ZnS, ZnSe, and some ternaries based on the bandgap energy; absorbers include CdSe, CdTe, CIGS, CZTS and some ternaries [19].

CHAPTER 3

SIMULATION METHODS

3.1. Introduction:

SILVACO (Silicon Valley Corporation) is an American company headquartered in Santa Clara, California. It is one of the top suppliers of expert software chains for computer-aided design and finite element simulation for electronics TCAD (Technology Computer Aided Design) applications. Microelectronics businesses use these tools for research, development, and device design [20].

With the goal of reducing development time and costs, TCAD simulators make it possible to simulate an electronic component's electrical behavior, which facilitates the evaluation and optimization of potential fixes to enhance device performance. All currently available simulators (such as ISE, SYNOPSIS, SILVACO, etc.) function according to the same idea [20].

This chapter will introduce the TCAD-SILVACO simulation software, its working theory, and its two simulation modules: ATLAS, which simulates component electrical behavior, and ATHENA, which simulates technological processes. We will also present the physical foundation of the ATLAS simulator's working concept, as well as a number of commands or instructions [21], [22].

3.2 Presentation of the SILVACO software package:

SILVACO presents a set of interactive simulation tools allowing the design and analysis of most Virtual Wafer Fab (VWF) semiconductor devices. The basic components of VWF (Figure 3.1) are: [20], [23]

1. Simulation tools (VWF CORE TOOLS): These tools simulate either their manufacturing processes or their electrical behaviors. The simulation tools are ATHENA, ATLAS, and SDUPEM3.

2. Interactive tools (VWF INTERACTIVE TOOLS): These tools are designed to be used interactively in constructing a single input file. They are based on a graphical user interface (GUI). Thus, the process of constructing the input file becomes more efficient. The interactive tools can be used either in conjunction with a set of files or as components integrated into the automation tool environment.

3. Automation tools (VWF AUTOMATION TOOLS): These tools allow users to conduct large-scale experimental studies to generate results for subsequent statistical analysis. The automation tools utilize distributed database technology and inter-process software development methods.

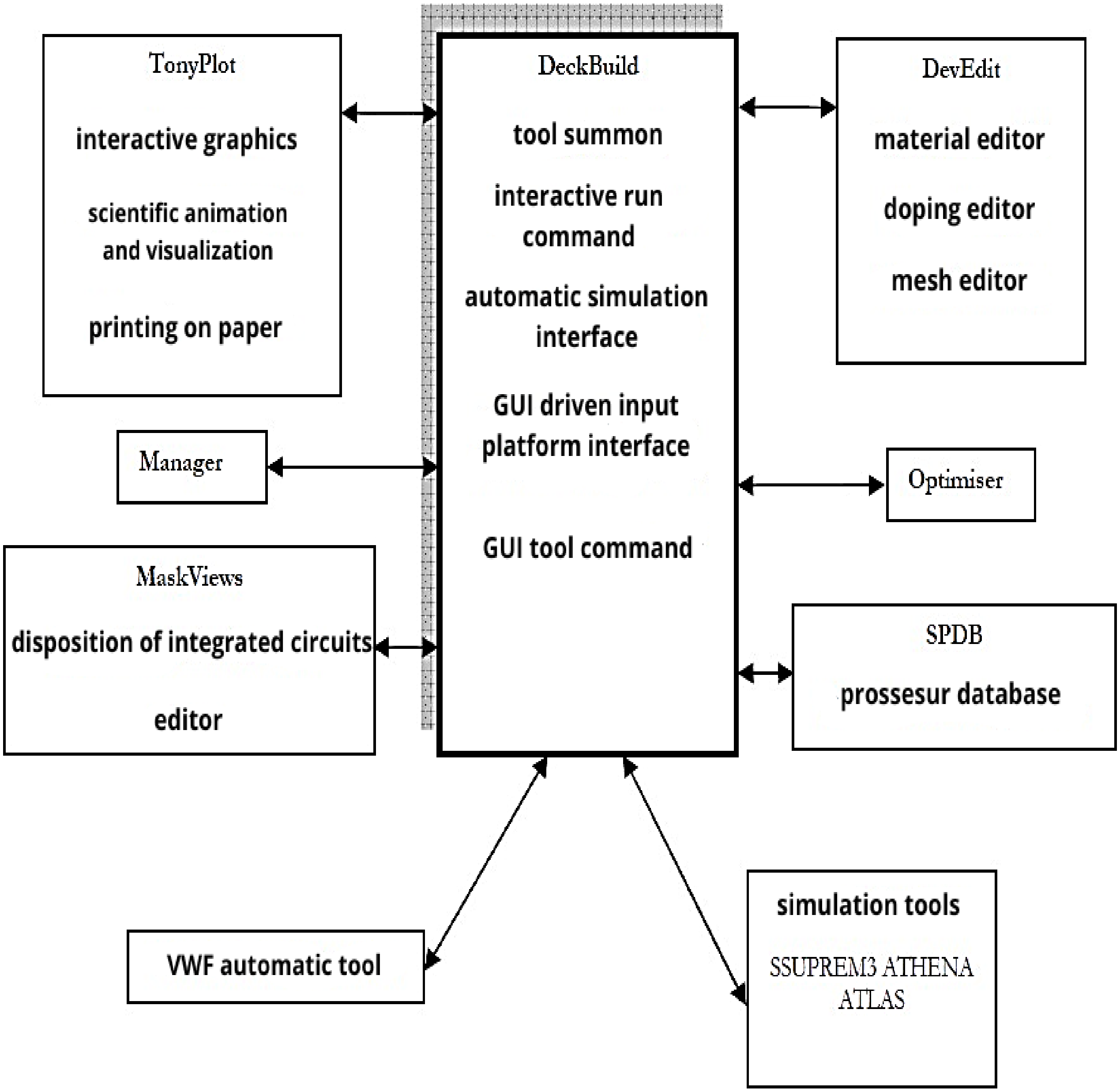

Figure 3.1: Organization chart of the VWF structure [20].

3.2.1 Simulation Tools:

- **ATLAS:** A physical simulator for 2D or 3D semiconductor devices that allows simulating the electrical behavior of specified semiconductor device structures.[20]
- **ATHENA:** A 2D process technology simulator that allows the development and optimization of semiconductor manufacturing processes (the various steps performed in a Clean Room). It provides a platform for simulating ion implantation, diffusion, etching, deposition, lithography, and oxidation. It replaces expensive experiments with simulations.[20]
- **SSUPREM3:** A 1D process simulator that allows the prediction of doping profiles and thicknesses produced by semiconductor processing. It is capable of simulating a complete flow of process steps.[20]

3.2.2 Interactive Tools:

- **DECKBUILD:** An environment where the simulation program is defined. DeckBuild provides assistance and support to avoid the learning of a generally complex command syntax. It also allows for automatic and convenient execution of programs and systematic saving of intermediate execution steps.[20]
- **TONYPLOT:** An environment where simulation results are visualized, including the structure of the component, distribution of various quantities within it, and electrical characteristics.
- **DEVEDIT:** An environment where the structure is drawn. New structures can be created or existing structures can be modified. It is also possible to define meshes or refine existing meshes. [20]
- **MASKVIEWS:** Mask drawing tool (layout editor).[20]
- **OPTIMIZER:** Optimizes the parameters of the structure to ultimately achieve the predefined parameter value.[20]
- **MANAGER:** File management tool used for VWF files.[20]
- **SPDB (Semiconductor Process Data Base):** This is a separate product and not an interactive tool, but it can be used with DeckBuild. It has been designed to store a large number of experimentally measured doping profiles as well as data describing the conditions of the experiments.

3.3 Presentation of ATLAS:

The ATLAS simulation software (by SILVACO) allows for 2D and 3D modeling of components. This tool is used for modeling semiconductor devices before their fabrication. It is highly valuable in the development of many research projects. In Figure 3.2, we present the input and output information for ATLAS.

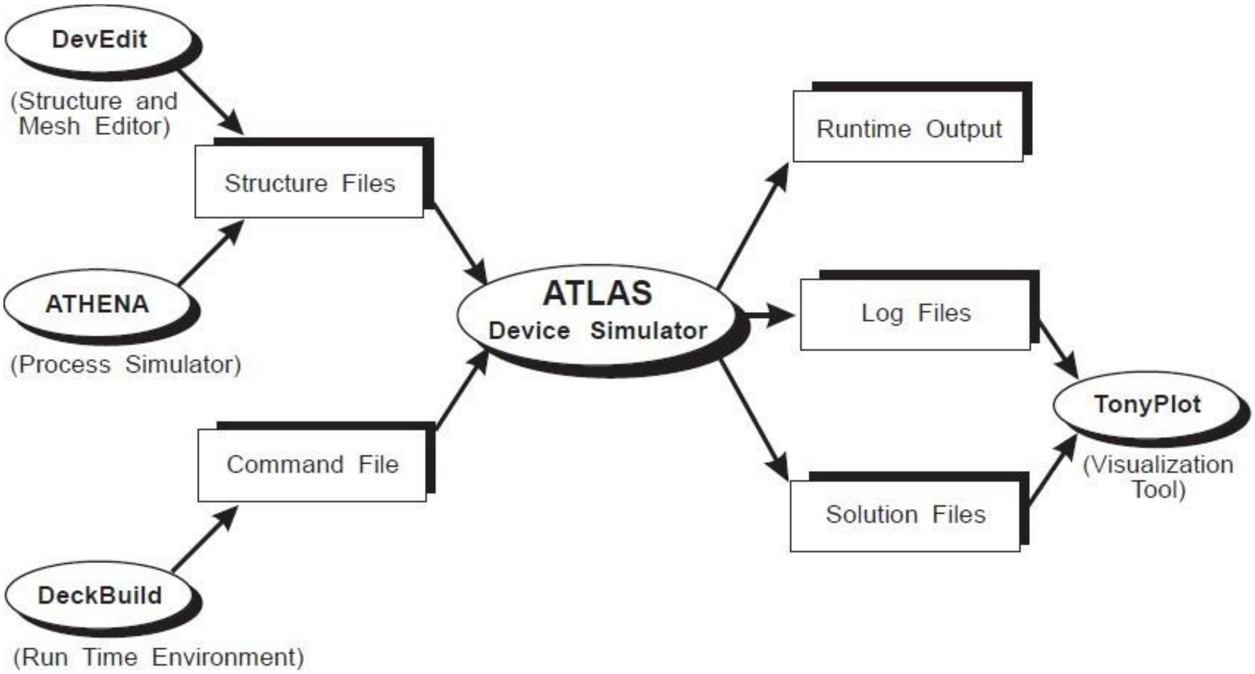

Figure 3.2: Entrances/exits of the Atlas simulator [24]**.**

Most simulations carried out by ATLAS use two input files [25]:

- A script file containing commands for ATLAS to execute (DECKBUILD environment used),
- A structure file defining the stack to be simulated.

The simulator provides 3 types of output files:

- A Runtime file that provides the progress, errors, and warning messages during the simulation.
- A log file storing all voltage and current values from the analysis of the simulated device (this is the electrical behavior file).
- A solution file storing 2D and 3D data corresponding to specific variable values inside the device, at a

given voltage.

The last two files are processed by the visualization tool TonyPlot. TonyPlot allows visualization of the structure in 2D or 3D and the requested electrical characteristics.

3.4 Commands in an ATLAS program:

Now we will present the order of fundamental commands in an ATLAS program (Table 3.1). Thus, there are five groups of commands, and these groups must be organized correctly. If the order is not respected, an error message appears, and the program does not execute correctly.

Group	Statements
1. Structure specification	MESH REGION ELECTRODE DOPING
2. Material models specification	MATERIAL MODELS CONTACT INTERFACE
3. Numerical method selection	METHOD
4. Solution specification	LOG SOLVE LOAD SAVE
5. Résultats analysis	EXTRACT TONYPLOT

Table 3.1: SILVACO-ATLAS control groups [24]**.**

3.4.1 Structure Specification:

This involves defining the most realistic structure. Constructing the structure consists of four steps: defining the mesh, defining regions, defining electrodes, and defining doping, according to [26]:

MESH: The mesh divides the simulated structure into small cells to solve the fundamental equations numerically. The mesh element used is the triangle. To ensure good accuracy during the simulation, the mesh should be as fine as possible. However, if the mesh is very fine, the computation time is very high because there are more elements to calculate. The general format for defining the mesh is:

X. MESH LOCATION = <VALUE> SPACING = <VALUE>
Y. MESH LOCATION = <VALUE> SPACING = <VALUE>
Figure 3.3 shows the mesh of our structure.

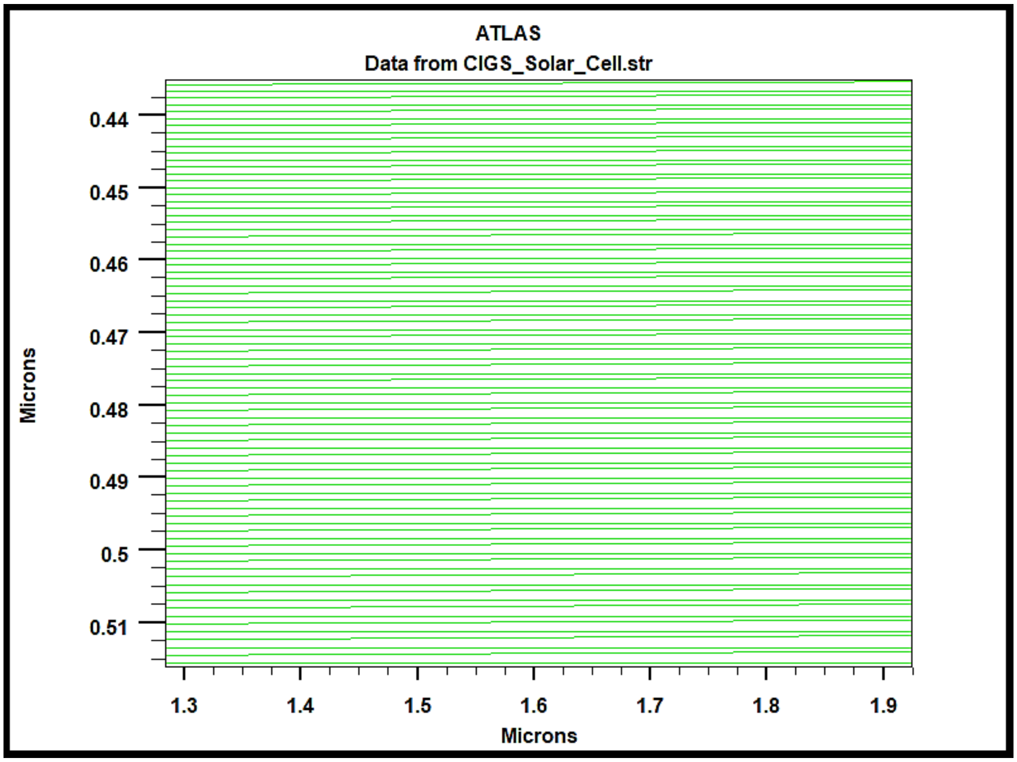

Figure 3.3: SILVACO-ATLAS control groups [21]**.**

REGION: After defining the mesh, it is necessary to define the regions, the format for defining regions with dimensions in micrometers is as follows:

REGION number = <integer><material_type><parameter position>

Figure 3.4 shows how to define materials for each region. Note that the color code indicates the material. The regions have horizontal lines to mark their boundaries.

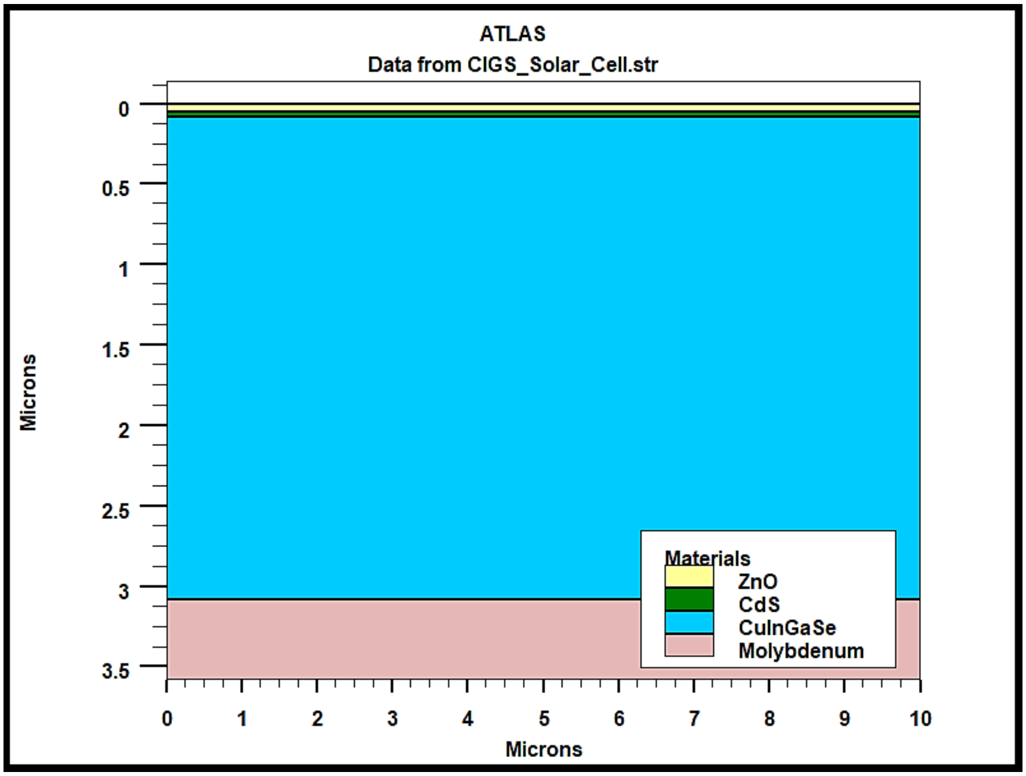

Figure 3.4: Definition of regions and materials by the ATLAS software.

ELECTRODE: Atlas has a limit of 50 electrodes that can be defined. The format for defining electrodes is as follows:

ELECTRODE name = <electrode name><parameter position>

The positions of the electrodes are localized by the following instructions:

X.MIN: Specifies the starting point of the electrode.

RIGHT: The position of the electrode is to the right of the structure (opposite: LEFT).

TOP: The position of the electrode is at the top of the structure (opposite: BOTTOM).

Figure 3.5 shows the position of the anode and cathode in the structure.

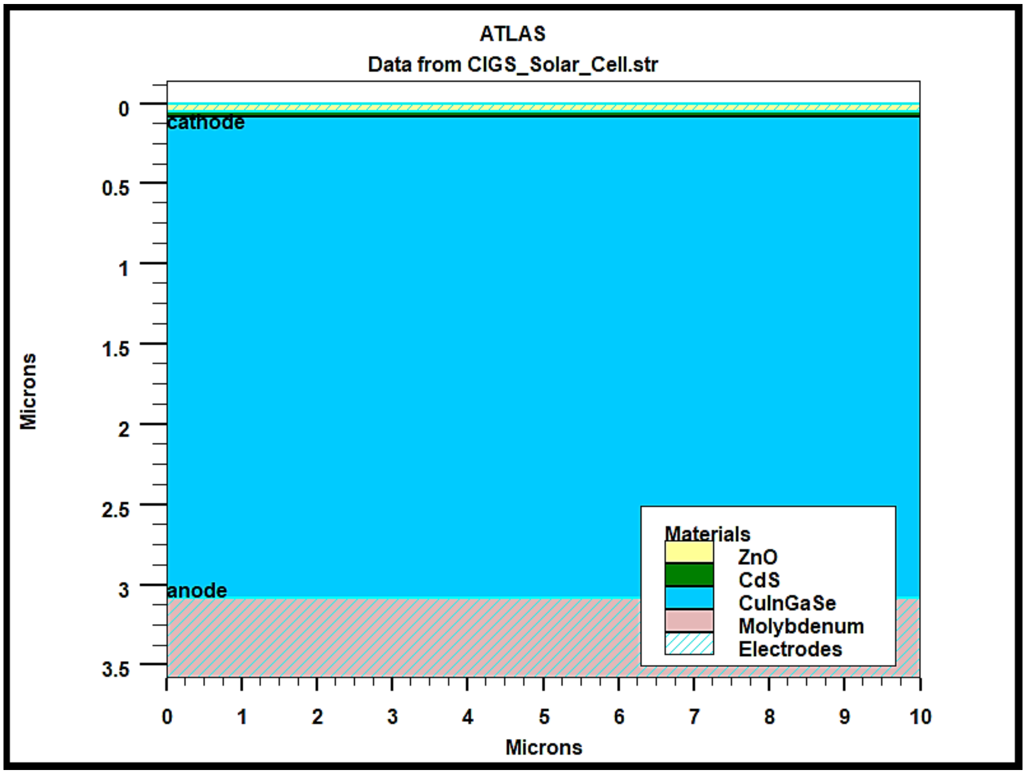

Figure 3.5: Definition of electrodes by the ATLAS software.

DOPING (doping definition): The final aspect of constructing the structure is doping. Doping can be of type n or p, and the distribution can be uniform, Gaussian, etc…

The format for declaring doping in ATLAS is as follows:

DOPING<distribution type><dopant type><parameter position>

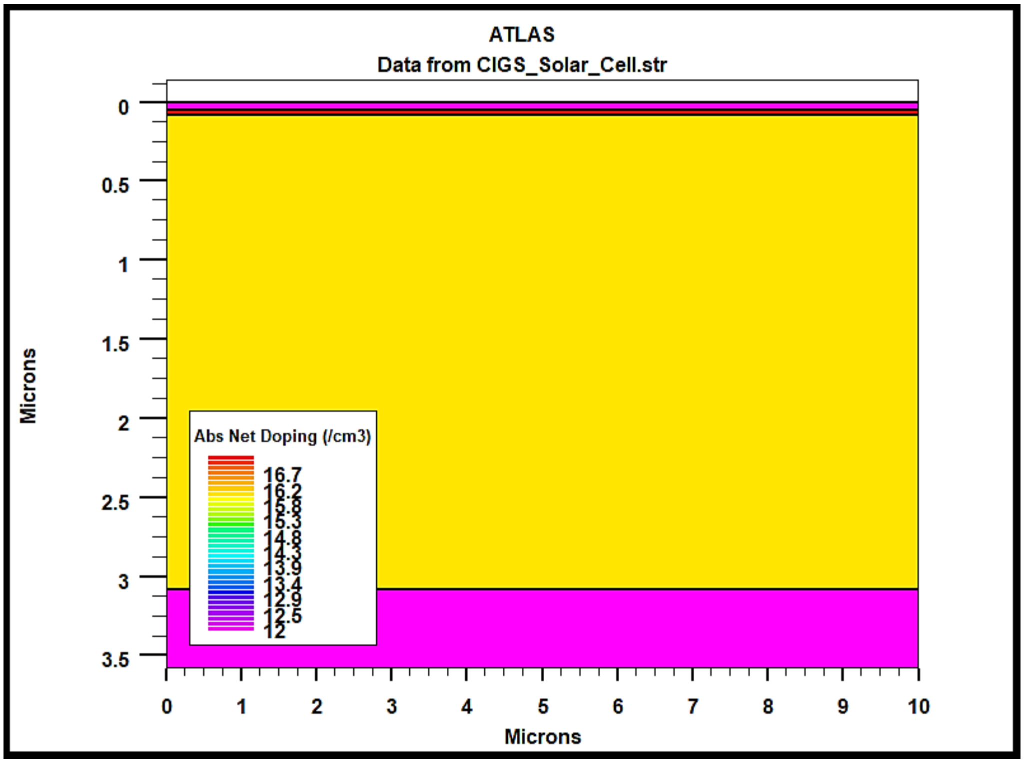

Figure 3.6: Distribution du dopage dans une structure par le logiciel ATLAS.

3.4.2 Specification of Models:

After constructing the framework, it's necessary to specify the physical models and define the materials. The specification of models and materials involves the following steps [22]:

MATERIAL: The format for declaring the material is as follows:

MATERIAL <location> <material definition>

Example:

MATERIAL MATERIAL=CdS EG300=2.42 PERMITTIVITY=10 \

AFFINITY=4.5 MUN=100 MUP=25 NC300=2.2e18 NV300=1.8e19.

Plusieurs autres paramètres peuvent être définis par la déclaration MATERIAL, comme exemples de ces paramètres : l’énergie du gap (EG300), la permittivité (PERMITIVITY), l’affinité (AFFINITY), la mobilité d'électrons (MUN), la mobilité de trous (MUP), la densité d’états en Ec (NC300) et la densité d’états en Ev (NV300).

- **MODELS**: These indicate the inclusions of various physical mechanisms (recombination, mobility, etc.). The choice of model depends on the materials chosen for the simulation.

The syntax for declaring the model is as follows:

MODEL <general parameters> <model parameters>

Example: SRH CONMOB FLDMOB.

SRH stands for the Shockley-Read-Hall model. CONMOB is the model for concentration-dependent mobility. FLDMOB is the model for electric field-dependent mobility.

CONTACT: There are also models related to the type of contact, either ohmic contact (default) or rectifying contact (Schottky contact). This contact is characterized by a work function such as:

Contact name = <integer> work = <integer>

Here is an example of contact declaration:

Contact name = anode workfun = 4.74

INTERFACE: The boundaries of semiconductors or insulators are determined by the "interface" declaration. The syntax is as follows:

INTERFACE <parameters> <interface_dimensions>

The following example demonstrates the use of the interface declaration:

Interface x.min=0 x.max=2000 y.min=0 y.max=0 s.n=1e3 s.p=1e3

Here, the values min and max determine the boundaries, and s.n and s.p represent the surface recombination velocities of electrons and holes at the interfaces.

BEAM <parameters>

Here is an example:

beam num=1 x.origin =1000 y.origin=-30 angle=90.0 power. file=AM0dis.spec reflects=1 front.refl back.refl

This declaration defines the number of light beams as 1, the ray origin for 2D optical sources; x.origin and y.origin are the x and y coordinates of the light beam origin in microns. A 90-degree angle of incidence indicates that the ray is perpendicular to the illuminated surface of the solar cell. power.file specifies the spectral source of the light by indicating the name of a .spec file containing intensity values of the spectrum used based on wavelengths.

The parameter reflects=1 specifies the number of reflections of the light beam. The front.refl and back.refl declarations enable the light ray to reflect off the front and back surfaces of the cell.

3.4.3 Selection of the numerical method:

The choice of numerical approach should be indicated once the material model accuracy has been specified. Three different numerical methods are employed in "Silvaco-Atlas" to solve systems of equations among the many available approaches:

- Gummel Method
- Newton's Method
- Block Method

The Gummel method is used for solving equations with a single unknown and fixed constant variables. The solution is obtained iteratively until completion. The Newton-Raphson method is the most widely used method in the Atlas program, employed for solving systems of equations with multiple unknowns. The third method is a combination of both techniques and is useful for mixed equation systems.

3.4.4. Solution Specification:

Finding the answers is required after choosing the numerical approach. The declarations LOG, SOLVE, LOAD, and SAVE provide the solution definition, as per :

Log: All terminal attributes are recorded in a data file using the Log instruction. The LOG instruction is used in the example that follows.

```
logoutfile = myoutputfile.log
```

The example demonstrates the recording of data in the file (myoutputfile.log).

Solve (Résoudre): The SOLVE instruction follows the LOG instruction. It performs a solution for one or more bias points. This declaration has the following basic format:

```
SOLVE <bias_points>
```

For example:

```
solve vanode=0 vstep=0.01 vfinal=2 name=anode
```

Load and Save: The LOAD command introduces, from an existing file, for each bias point, the previous solutions as an initial guess. The SAVE instruction allows the recording of all obtained information for a node in an output file. The instructions for load and save are as follows:

```
LOAD INFILE=<filename>
```

SAVE OUTFILE=<filename>

3.4.5. Analysis of the results:

Once the solution has been found for a semiconductor device problem, the information can be displayed graphically. According to [20]:

- **EXTRACT:** Commands of this type are used to extract specific values of parameters from both log files or structure.
- **TONYPLOT:** Starts the "Tony Plot" program allowing graphical representation of the data.

3.5. The Basic Semiconductor Equations in ATLAS-SILVACO:

This device simulator is based on solving the Poisson equation as well as the electron and hole continuity equations simultaneously. It calculates a sequence of finite elements that represent the concentration of electrons and holes as well as the electrostatic potential value at every instant and place in space [26]. A link between the potential and the carrier density is shown by the Poisson equation:

$$\Delta \mathrm{V} = -\frac{q}{\varepsilon}[\mathrm{p} - \mathrm{n} + \mathrm{N_D}^{+} - \mathrm{N_A}^{-}] \qquad (3.1)$$

Where V is the potential, q is the elementary charge of electrons, ε is the dielectric constant, ND+ and NA- are the concentrations of ionized donor and acceptor dopants, and n and p are the densities of electrons and holes.

The continuity equations for electrons and holes are [22]:

$$\frac{\partial \mathrm{n}}{\partial \mathrm{t}} = +\frac{1}{q} div\overrightarrow{\mathrm{J_n}} + \mathrm{G_n} - \mathrm{R_n} \qquad (3.2)$$

$$\frac{\partial \mathrm{p}}{\partial \mathrm{t}} = -\frac{1}{q} div\overrightarrow{\mathrm{J_p}} + \mathrm{G_p} - \mathrm{R_p} \qquad (3.3)$$

Where Jn and Jp are the current densities of electrons and holes, Gn and Gp are the generation rates for electrons and holes, Rn and Rp are the recombination rates for electrons and holes.

Derivations based on Boltzmann transport theory have shown that the current densities in the continuity equations can be defined by the drift-diffusion model.

The current densities are expressed in two terms. The first corresponds to the drift of charges by the electric field, the second corresponds to the diffusion of carriers [22].

$$\overrightarrow{J_n} = qn\mu_n\vec{E} \times qD_n\overrightarrow{grad(n)} \qquad (3.4)$$

$$\overrightarrow{J_p} = qn\mu_p\vec{E} \times qD_p\overrightarrow{grad(p)} \qquad (3.5)$$

$$\vec{E} = -\overrightarrow{grad(V)} \qquad (3.6)$$

Where Dn and Dp are the diffusion coefficients. They are directly related to the carrier mobilities by the Einstein relation:

$$Dn = \frac{kT}{q}\,\mu n \qquad (3.7)$$

$$Dp = \frac{kT}{q}\,\mu p \qquad (3.8)$$

3.6. conclusion:

This chapter has provided some basic information on programming with Silvaco-Atlas, with several specific aspects of programming methodology presented, including program structure, specification of material parameters and physical models, and selection of numerical methods.

CHAPTER 4

RESULTS AND DESCUSSION

4.1. Introduction:

In this chapter, we will simulate a solar cells in CIGS and CZTS, we will optimize the output performance of this solar cells when trying to find the parameters optimal of each region constituting the cell, we will calculate the values of photovoltaic parameters of the solar cell such as short-circuit current, open-circuit voltage, form factor and efficiency. Cell optimization solar energy includes the study of the influence of the concentrations of donors and acceptors and the thicknesses of the layers on the yield in order to obtain a structure leading to the yield maximum.

4.2. Studied solar cell structures:

The basic structure of a CIGS and CZTS thin film solar cell comprises several layers, as illustrated in Figure 4.1.

The most commonly used substrate is soda lime silicate glass, which is coated on one side with molybdenum (Mo), serving as the rear metallic contact (anode). The heterojunction is formed between CIGS and aluminum-doped ZnO semiconductors (ZnO:Al), featuring a double interface layer composed of CdS and intrinsic ZnO (ZnO-i). The CIGS and CZTS layers exhibits p-type doping due to intrinsic defects, while the ZnO layer is n-type, achieved through the incorporation of aluminum (Al). The CIGS/CZTS layer functions as the absorber.

The construction of this structure within the Atlas simulator involves four steps: defining the mesh, regions, electrodes, and doping. The structure is exposed to an incident light power of 0.1 W/cm\(^2\).

Figure 4.1: Shematic structure of CdS/CIGS or CdS/CZTS solar cells

4.3. Study of CdS/CIGS:

4.3.1. effect of CIGS thickness on CdS/CIGS solar cell parameters:

The effect of CIGS thickness with a fixed carrier concentration at 10^16 cm-3 on the photovoltaic parameters of the solar cell are shown in Table 4.1 and Figure 4.2.

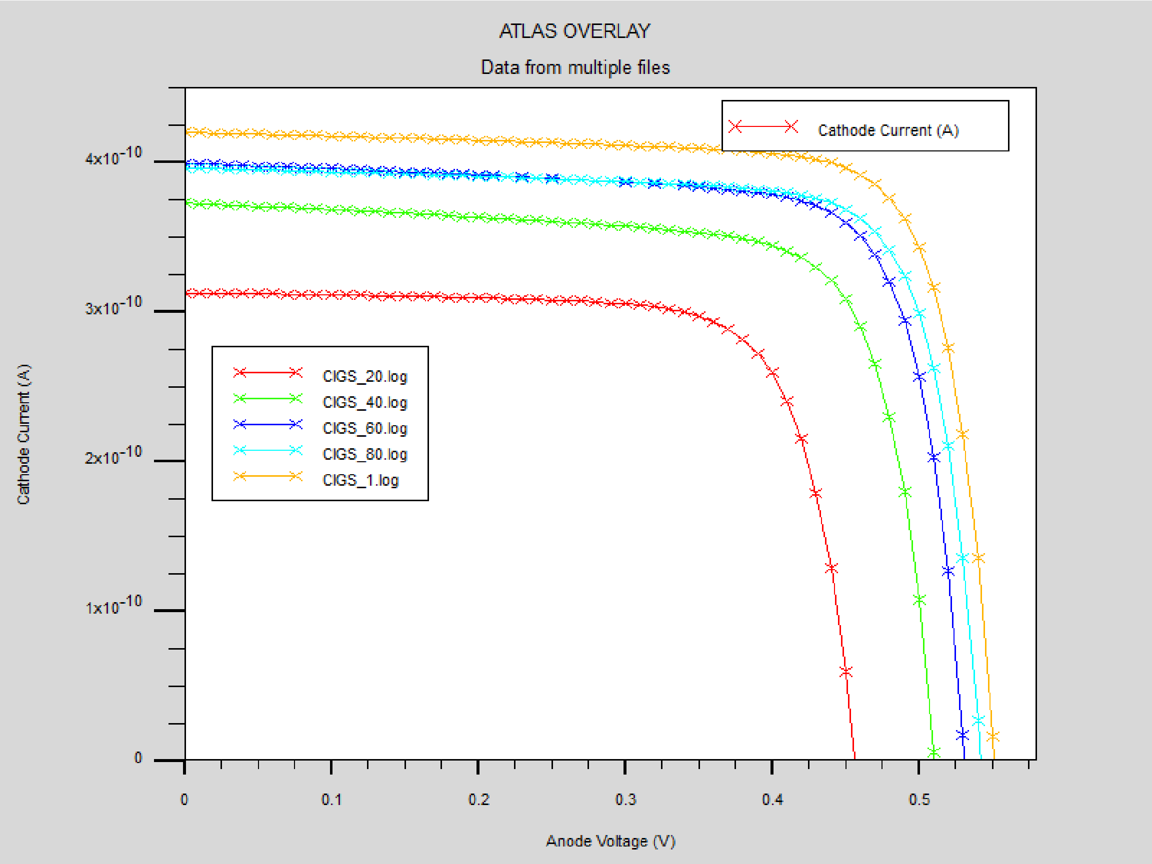

Figure 4.2: I-V characteristics of CdS/CIGS with different CIGS thickness values

We note that as the thickness of the CIGS increases, the yield increases. Due to the fact as the thickness of the CIGS increases, more carriers are photo generated which result in a higher current. Furthermore, in Figure 4.3, the optimal thickness of the absorbent layer is of around 1 µm.

CIGS thickness (µm)	Efficiency (%)	Fill Factor (%)	V_{oc} (V)	I_{sc} (mA/cm^2)
0.20	10.6927	75.08603	0.45608	31.2237
0.40	14.157	74.50473	0.5104	37.2286
0.60	16.1737	76.34752	0.53109	39.8886
0.80	16.6516	77.62426	0.54175	39.5969
1.00	18.0877	78.23709	0.5509	41.9626

Table 4.1: Photovoltaic parameters of the CdS/CIGS solar cell as a function of the thickness of the CIGS layer.

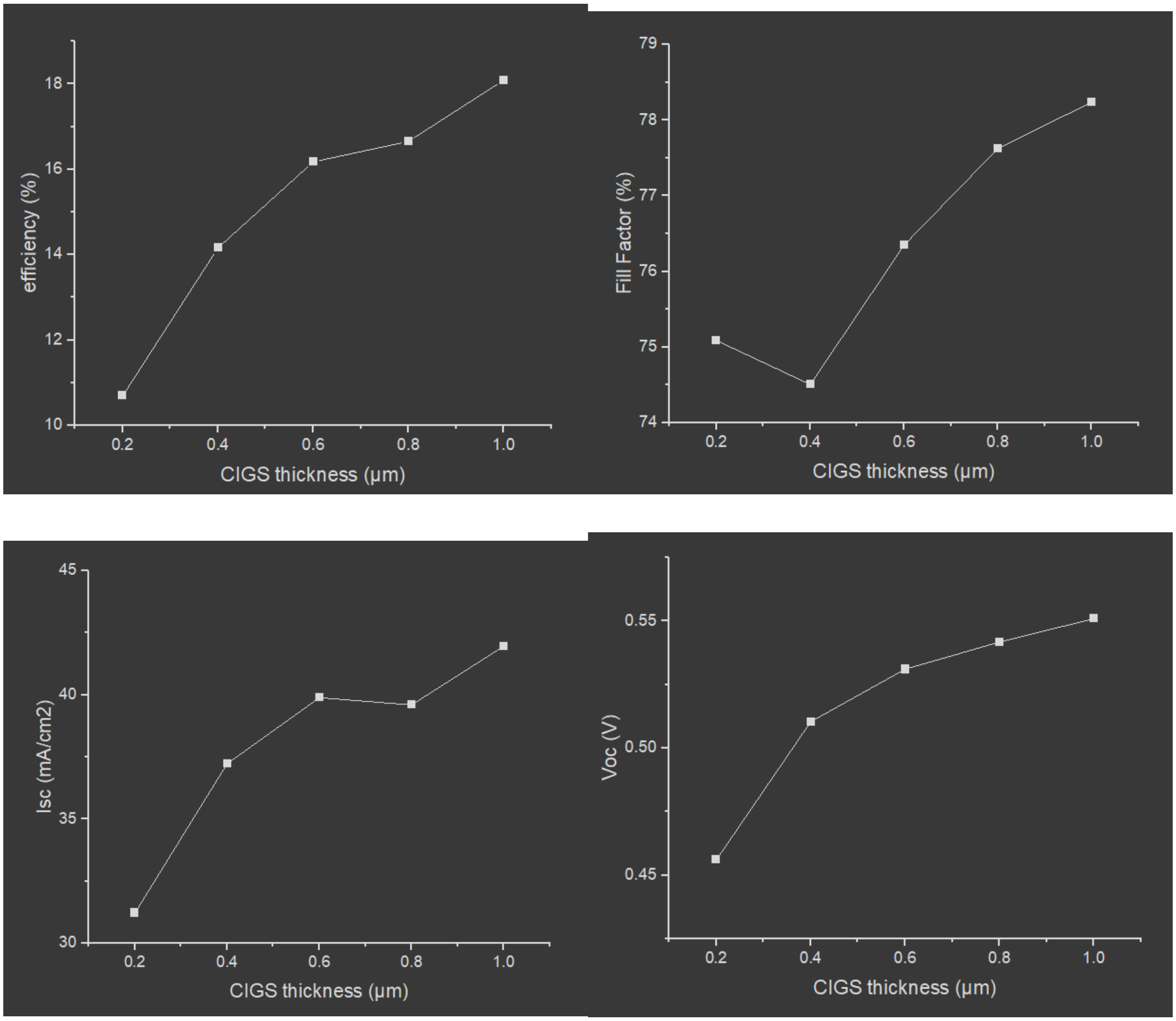

Figure 4.3: Photovoltaic parameters of the CdS/CIGS solar cell as a function of the thickness of the CIGS layer.

4.3.2. Effect of CIGS doping on CdS/CIGS solar cell parameters:

The variation of the photovoltaic parameters of the solar cell depending on the concentration of acceptors in the CIGS layer with a thickness of 1 um are shown in the table 4.2 and in Figure 4.4 and Figure 4.5.

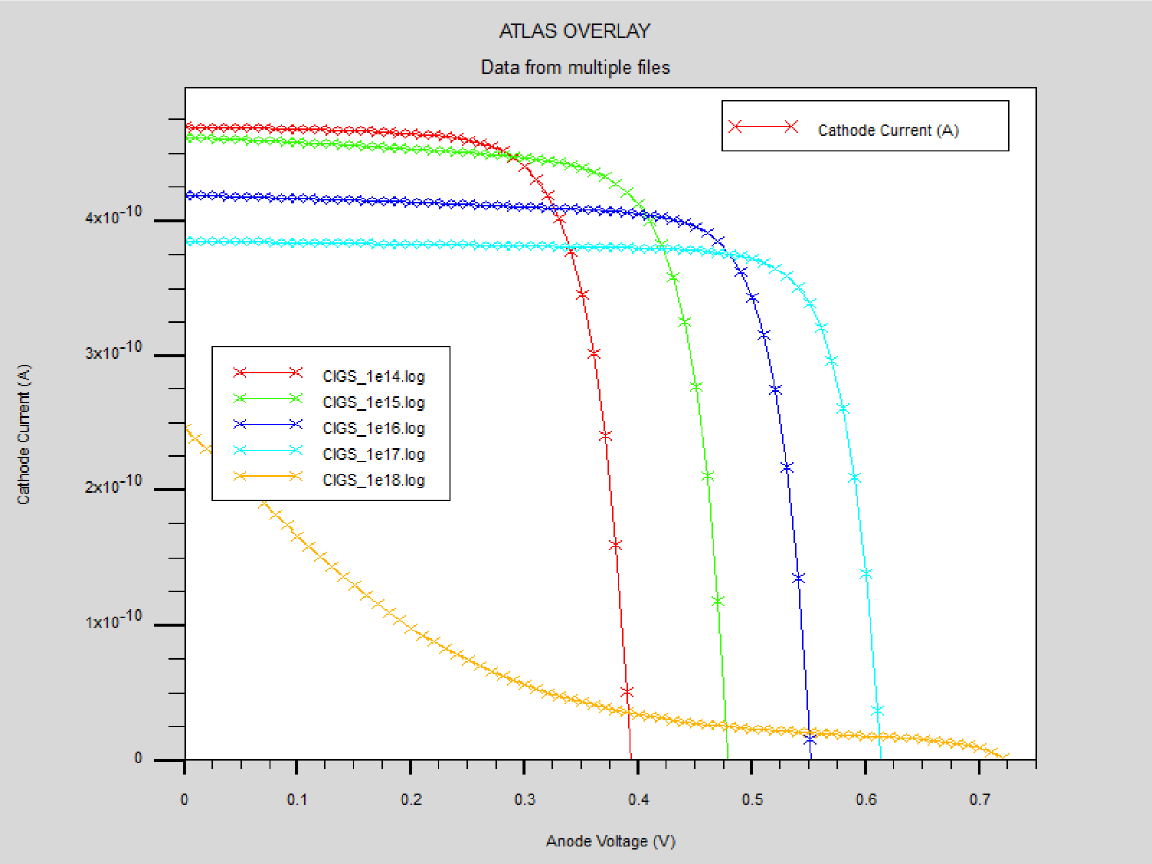

Figure 4.4: I-V characteristics of CdS/CIGS with different CIGS doping values

Therefore, a concentration of acceptors of the CIGS layer of 10^17 cm-3 is used as an optimal value.

CIGS Doping (cm^{-3})	Efficiency (%)	Fill Factor (%)	V_{oc} (V)	I_{sc} (mA/cm^2)
10^14	13.4078	72.46788	0.39352	47.0163
10^15	16.5115	74.51938	0.47916	46.2424
10^16	18.0877	78.23709	0.55095	41.9626
10^17	19.0482	80.65293	0.61267	38.5486
10^18	1.9791	11.1178	0.72315	24.616

Table 4.2: Photovoltaic parameters of the CdS/CIGS solar cell as a function of the doping of acceptors in the CIGS layer.

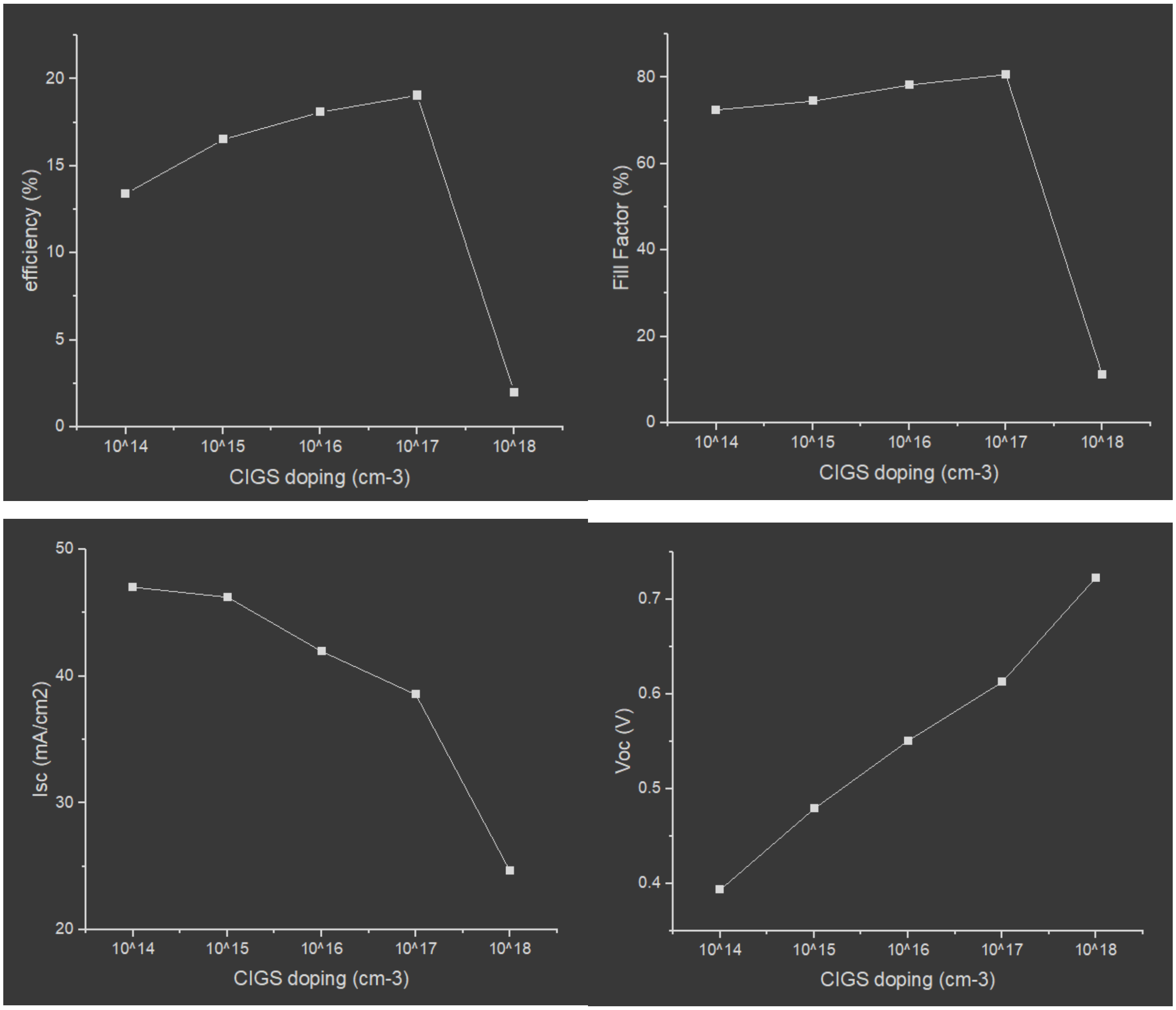

Figure 4.5: Photovoltaic parameters of the CdS/CIGS solar cell as a function of the doping of acceptors in the CIGS layer.

4.4. Study of CdS/CZTS:

4.4.1. Effect of CZTS thickness on CdS/CZTS solar cell parameters:

The effect of CZTS thickness with a fixed carrier concentration at 10^16 cm-3 on the photovoltaic parameters of the solar cell are shown in Table 4.3 and Figure 4.6.

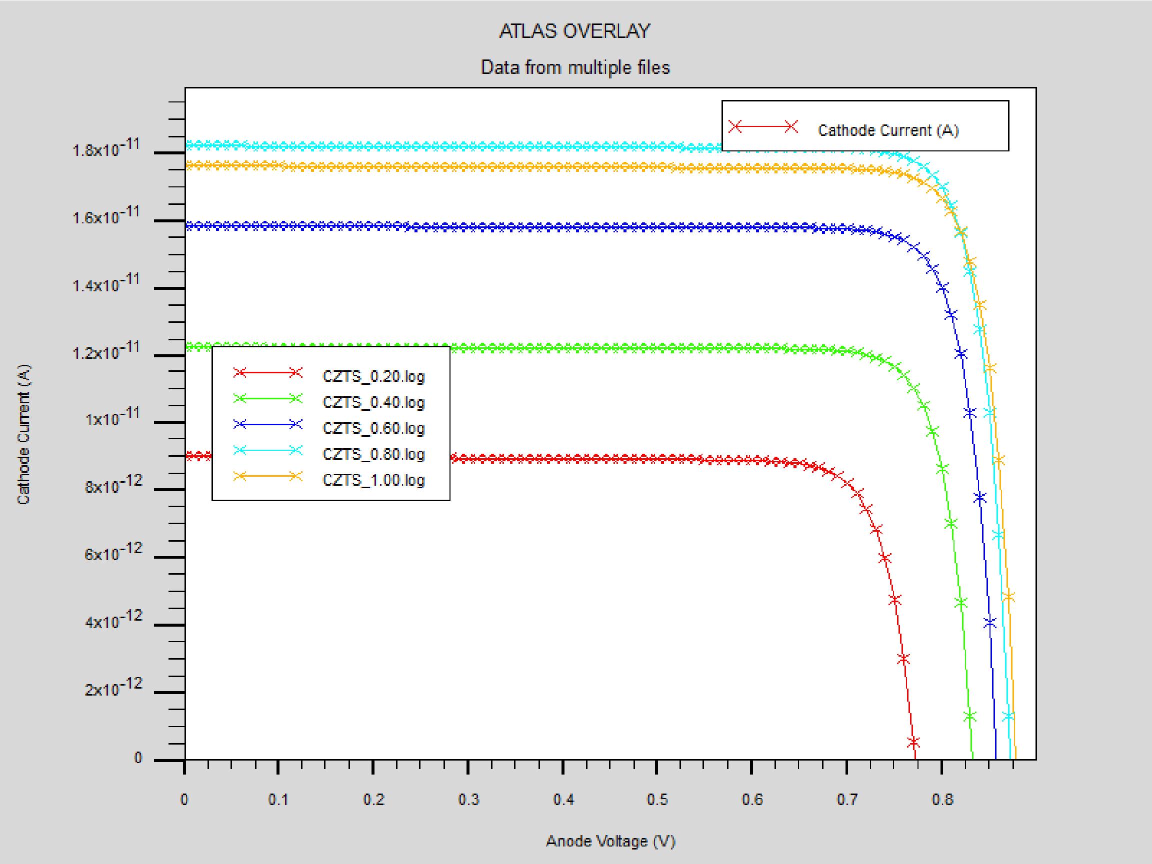

Figure 4.6: I-V characteristics of CdS/CZTS with different CZTS thickness values

We note that as the thickness of the CZTS increases, the yield increases. Due to the fact as the thickness of the CZTS increases, more carriers are photo generated which result in a higher current. Furthermore, in Figure 4.7, the optimal thickness of the absorbent layer is of around 0.8 um.

CZTS Thickness (µm)	Efficiency (%)	Fill Factor (%)	V_{oc} (V)	I_{sc} (mA/cm^2)
0.20	5.82924	83.61495	0.77152	9.03606
0.40	8.76159	85.75358	0.83264	12.2708
0.60	11.7459	86.28941	0.85759	15.8726
0.80	13.7601	86.4766	0.87169	18.2541
1.00	13.4193	86.51759	0.8782	17.6617

Table 4.3: Photovoltaic parameters of the CdS/CZTS solar cell as a function of the thickness of the CZTS layer.

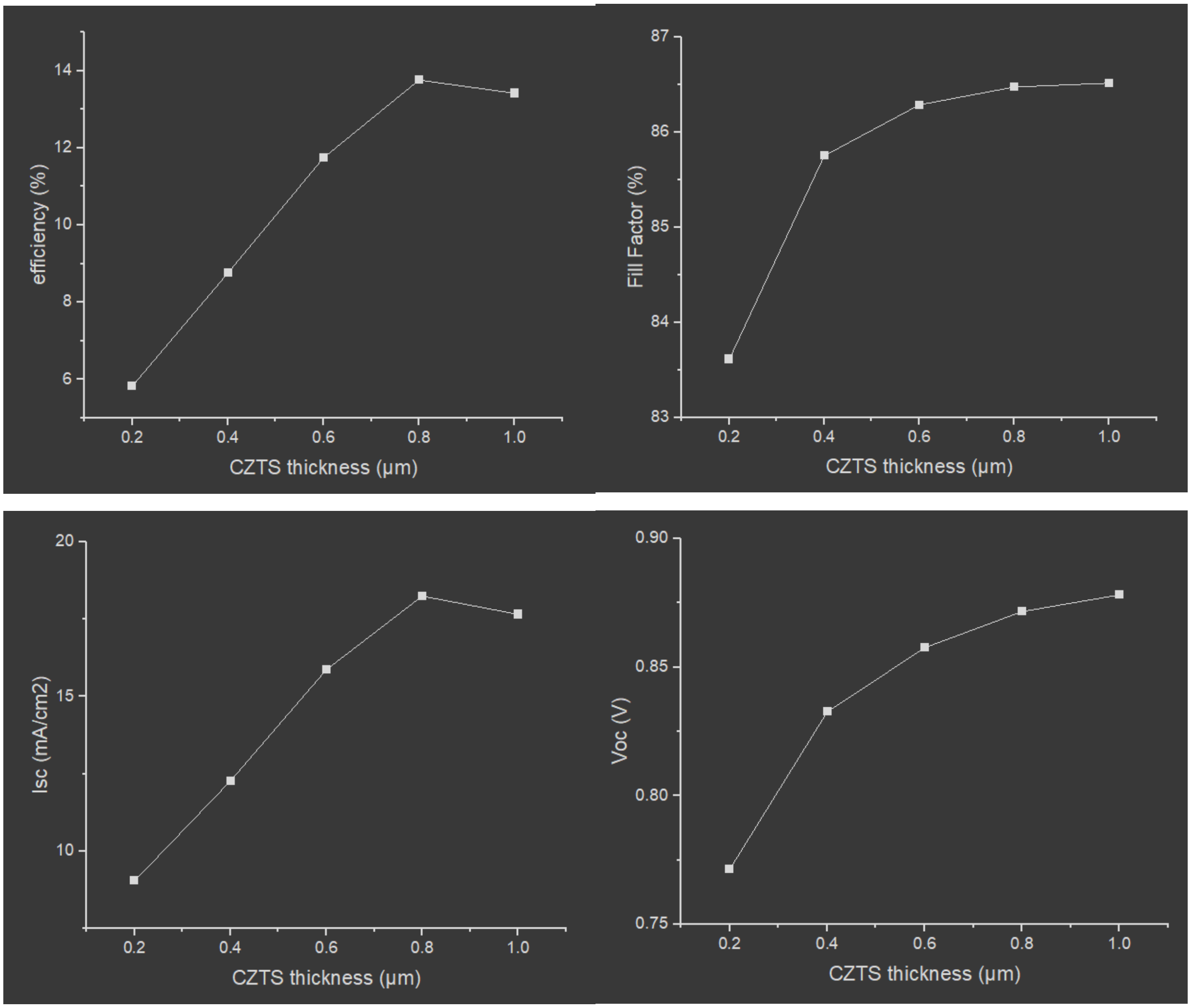

Figure 4.7: Photovoltaic parameters of the CdS/CZTS solar cell as a function of the thickness of the CZTS layer.

4.4.2. Effect of CZTS doping on CdS/CZTS solar cell parameters:

The variation of the photovoltaic parameters of the solar cell depending on the concentration of acceptors in the CZTS layer with a thickness of 0.8 um are shown in the table 4.4 and in Figure 4.8 and Figure 4.9.

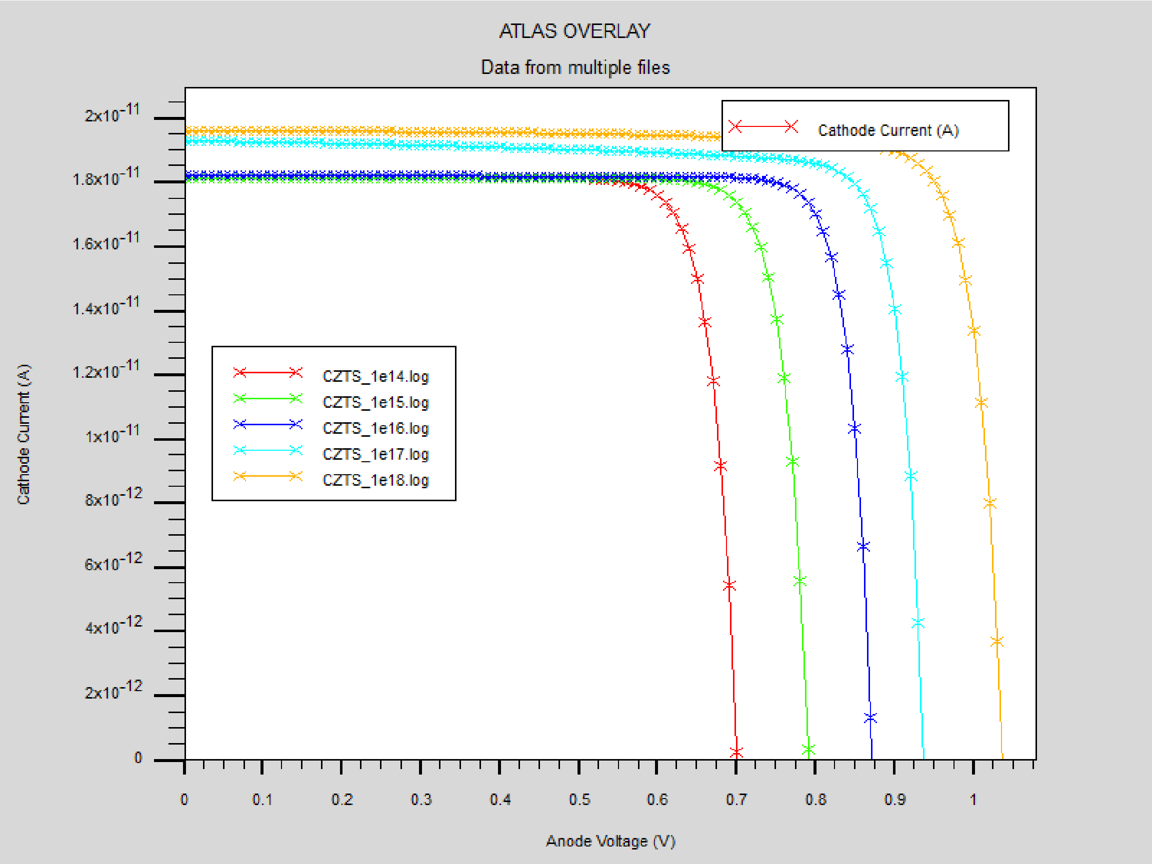

Figure 4.8: I-V characteristics of CdS/CZTS with different CZTS doping values

Therefore, a concentration of acceptors of the CZTS layer of 10^18 cm-3 is used as an optimal value.

CZTS Doping (cm^{-3})	Efficiency (%)	Fill Factor (%)	V_{oc} (V)	I_{sc} (mA/cm^2)
10^14	10.6094	83.41533	0.70033	18.161
10^15	12.1811	84.83075	0.79042	18.1666
10^16	13.7601	86.4766	0.87169	18.2541
10^17	15.2844	84.47941	0.93641	19.321
10^18	17.2928	84.93701	1.03621	19.6481

Table 4.4: Photovoltaic parameters of the CdS/CZTS solar cell as a function of the doping of acceptors in the CZTS layer.

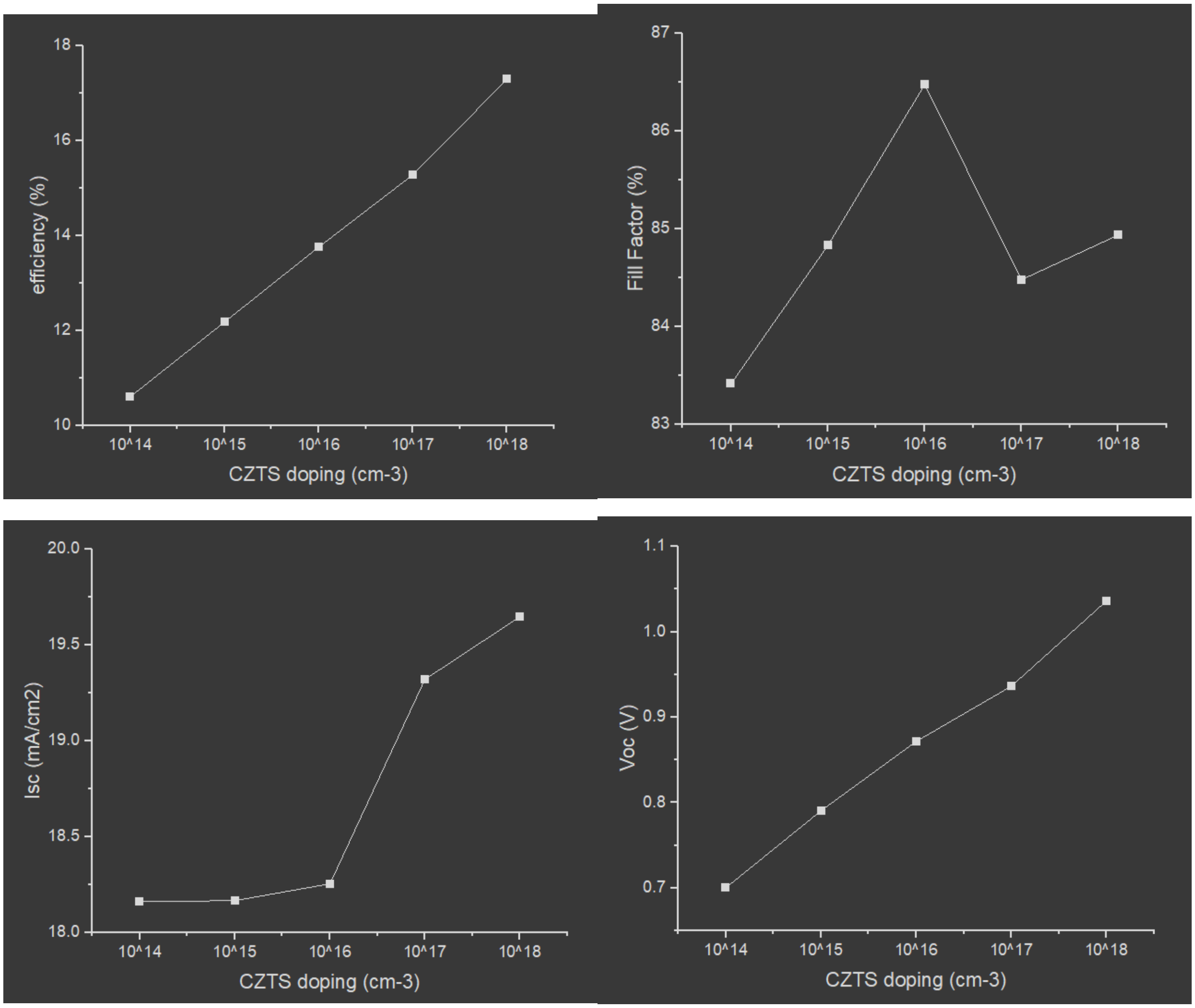

Figure 4.9: Photovoltaic parameters of the CdS/CZTS solar cell as a function of the doping of acceptors in the CZTS layer.

4.5. Study of CdS effect on the performance of the studied solar cells

In this study, we examine the effects of varying the thickness and doping concentration of the CdS layer on the performance of CIGS and CZTS thin film solar cells. Our findings indicate that modifications to these parameters do not result in significant changes to the overall efficiency of both studied solar cells. This suggests that the thickness and doping level of the CdS layer have a minimal impact on the device performance. To further illustrate this point, we will use CIGS (Copper Indium Gallium Selenide) as an example to construct a CdS/CIGS solar cell. By systematically varying the parameters of the CdS layer, including its thickness and doping concentration, we aim to observe the resulting effects on the overall performance of the solar cell. Preliminary results confirm that changes in these parameters of the CdS layer have an insignificant impact on the efficiency and performance of the CdS/CIGS solar cell. This reinforces the notion that the CdS layer's characteristics can be adjusted without adversely affecting the solar cell's functionality, providing greater flexibility in the design and fabrication processes.

4.5.1. Effect of CdS thickness on the studied solar cells:

Photovoltaic parameters of the solar cell in CIGS depending on the thickness of donors in the CdS layer.

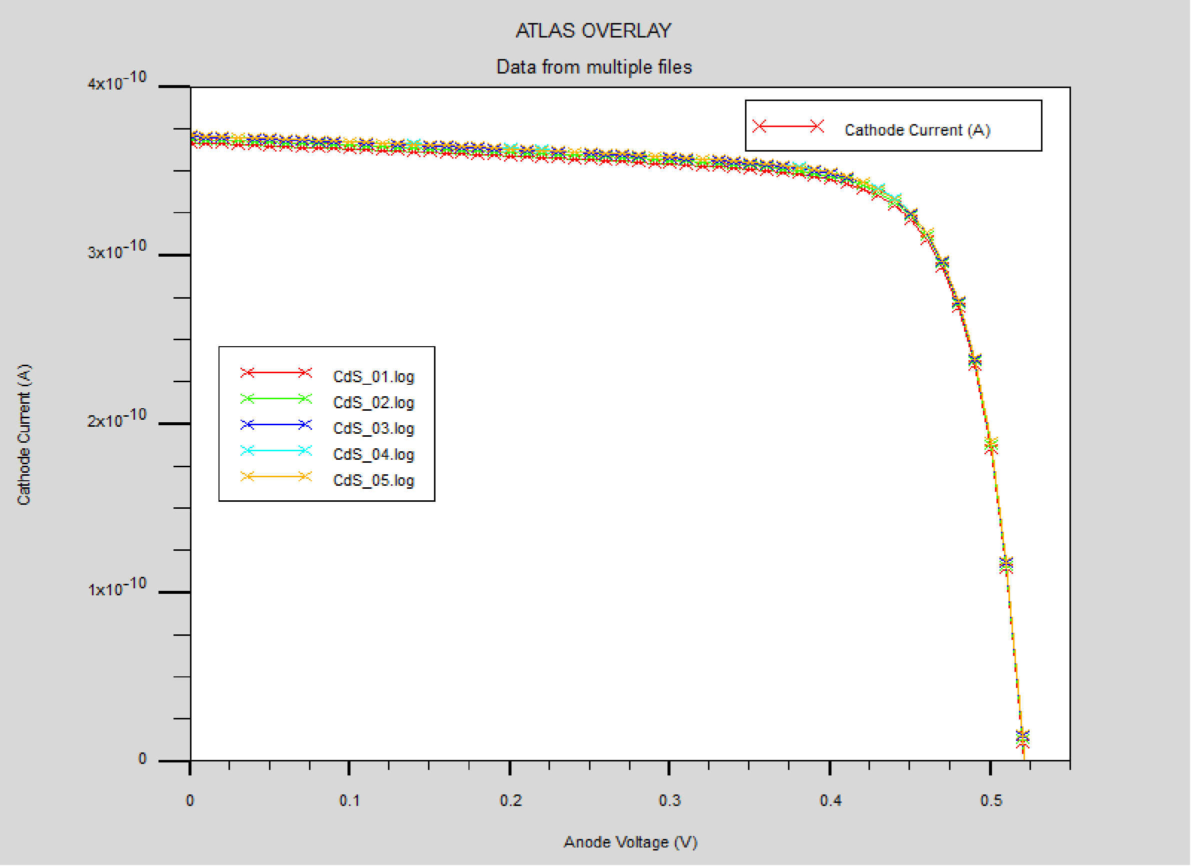

Figure 4.10: I-V characteristics of CdS/CIGS with different CdS thickness values

Despite the inherent differences in these solar cell configurations, our findings indicated that changes in CdS thickness level resulted in marginal variations in photovoltaic performance for both systems. Therefore, we adopted the optimal thickness from studying CdS/CIGS solar cell which 0.4µm for use in both CdS/CIGS and CdS/CZTS configurations.

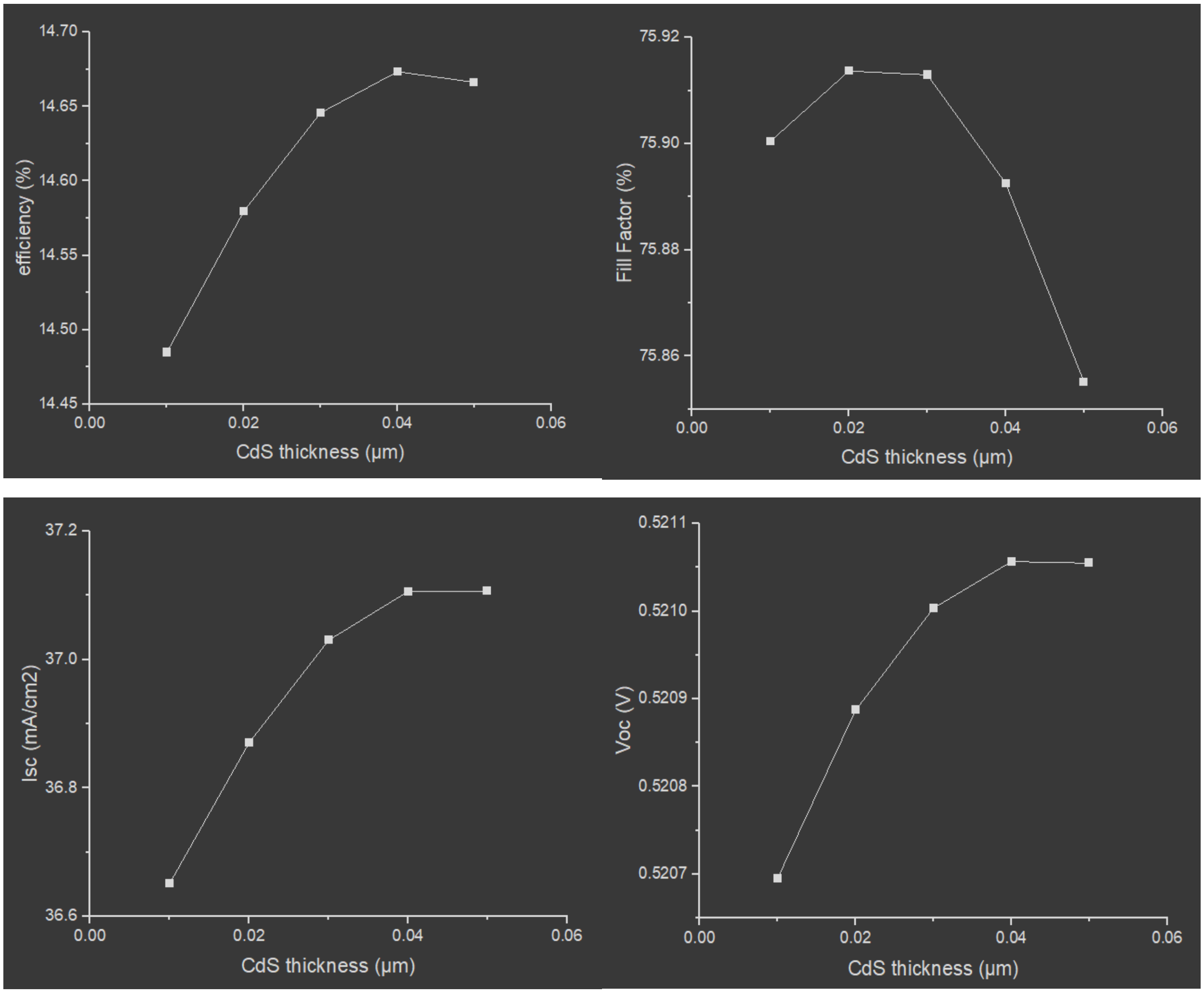

Figure 4.11: Effect of CdS thickness on CdS/CIGS solar cell performance

4.5.2. Effect of CdS doping on the studied solar cells:

Photovoltaic parameters of the solar cell in CIGS depending on the concentration of donors in the CdS layer.

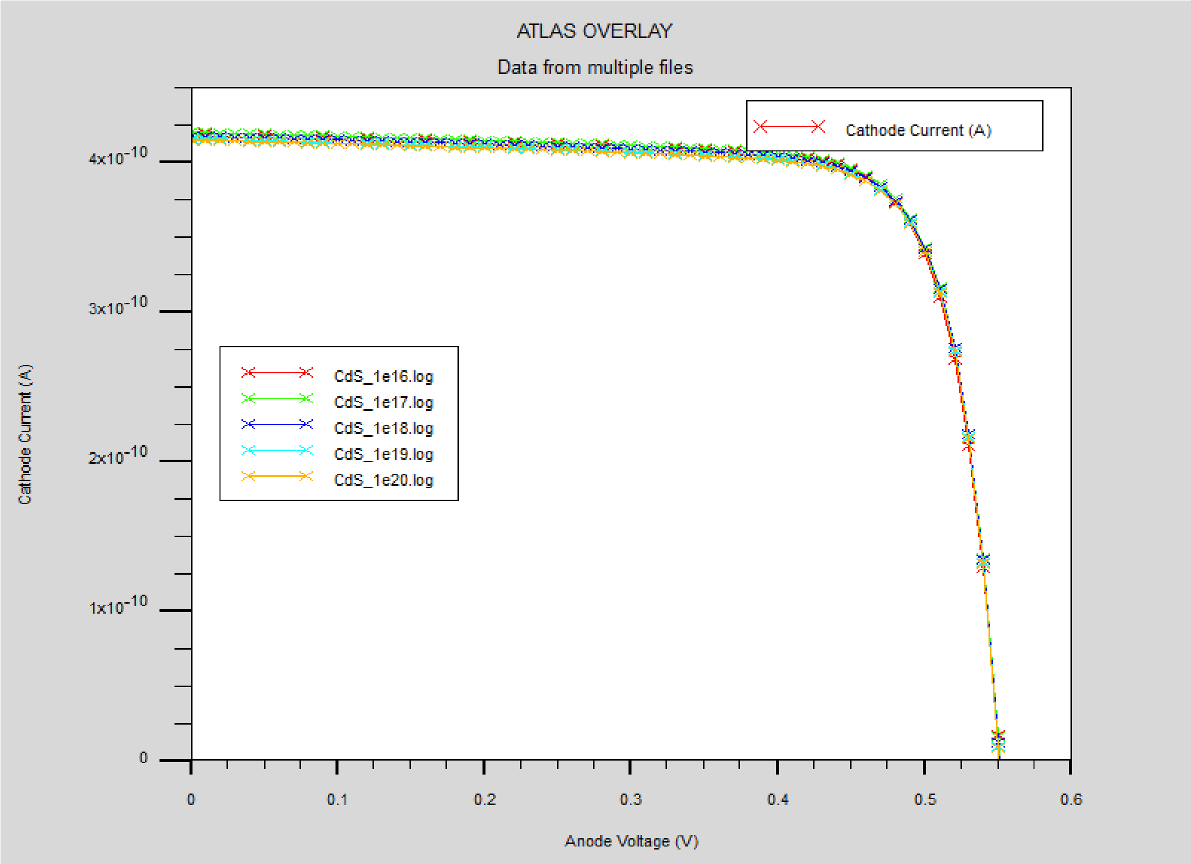

Figure 4.12: I-V characteristics of CdS/CIGS with different CdS doping values

Despite the inherent differences in these solar cell configurations, our findings indicated that changes in CdS doping level resulted in marginal variations in photovoltaic performance for both systems. Therefore, we adopted the optimal doping from studying CdS/CIGS solar cells which is 10^17cm^{-3} for use in both CdS/CIGS and CdS/CZTS configurations.

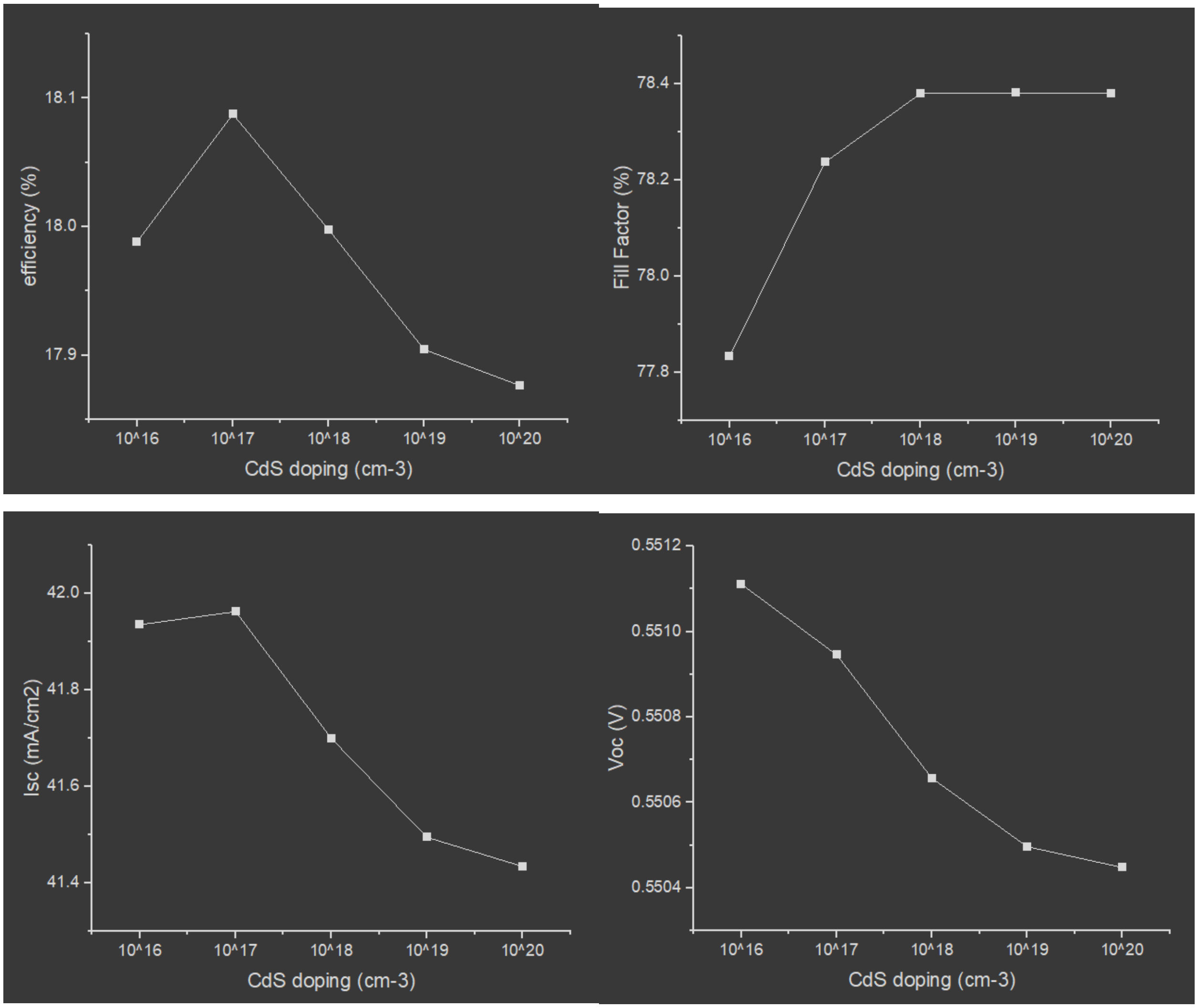

Figure 4.13: Effect of CdS doping on CdS/CIGS solar cell performance

4.6. The optimal parameters of the studied solar cell:

4.6.1. CdS/CIGS:

The obtained optimal physical parameters of CIGS in the CdS/CIGS solar cell are provided in table 4.5:

Optimal thickness (µm)	Optimal doping (cm^{-3})
1.00	10^17

Table 4.5: optimal physical parameters of CIGS

The photovoltaic parameters of the optimized solar cell are grouped in the table 4.6:

Parameters	Efficiency (%)	Fill Factor (%)	V_{oc} (V)	I_{sc} (mA/cm^2)
values	19.0482	80.65293	0.61267	38.5486

Table 4.6: optimal photovoltaic parameters of CdS/CIGS solar cell

4.6.2. CdS/CZTS:

The obtained optimal physical parameters of CZTS in the CdS/CZTS solar cell are provided in table 4.7:

Optimal thickness (µm)	Optimal doping (cm^{-3})
0.80	10^18

Table 4.7: optimal physical parameters of CZTS

The photovoltaic parameters of the optimized solar cell are grouped in the table 4.8:

Parameters	Efficiency (%)	Fill Factor (%)	V_{oc} (V)	I_{sc} (mA/cm^2)
values	17.2928	84.93701	1.03621	19.6481

Table 4.8: optimal photovoltaic parameters of CdS/CZTS solar cell

4.6.3. Comparison between the optimal values of the studied solar cells:

Figure 4.14 represents the I-V characteristics of two CdS solar cells with layers in CIGS and CZTS.

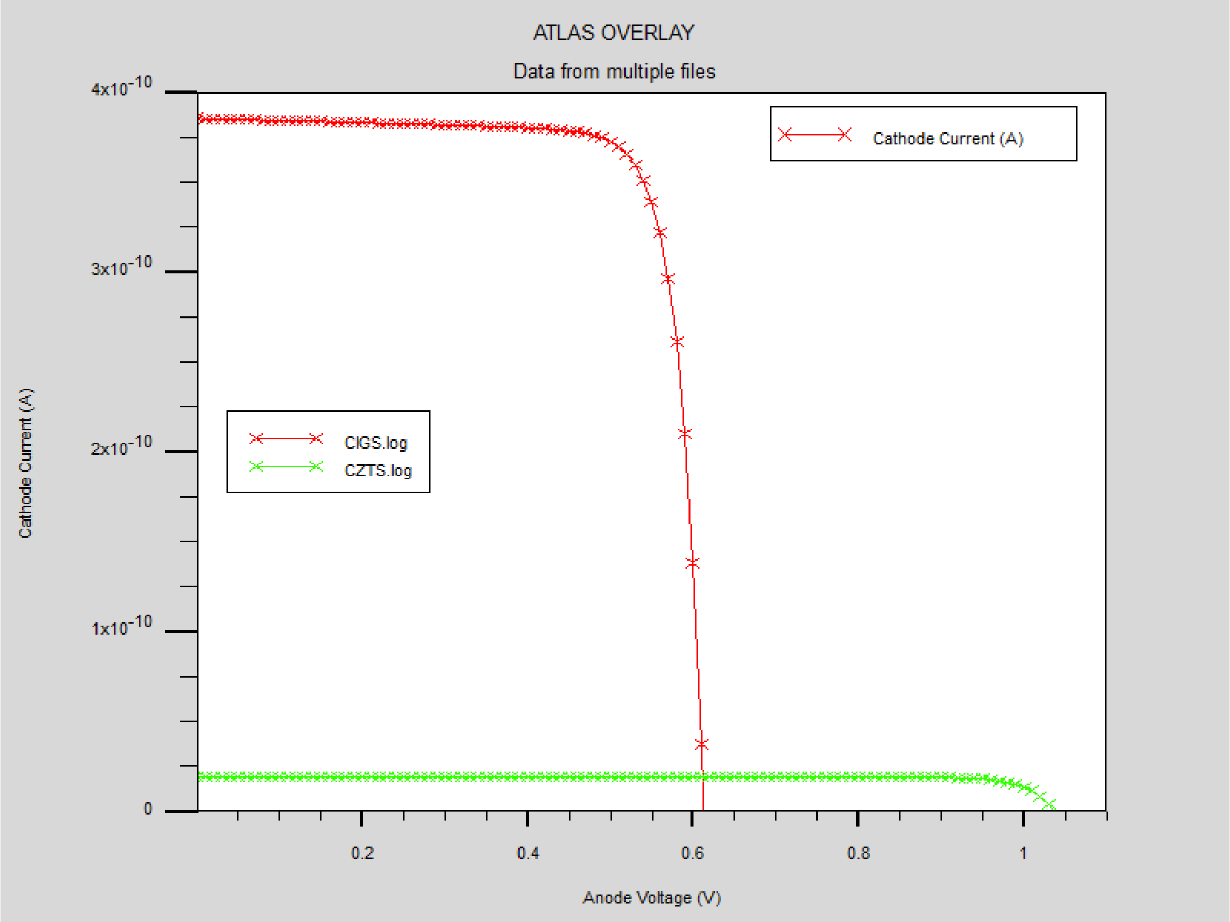

Figure 4.14: Comparison between I-V characteristics of CdS/CIGS and CdS/CZTS solar cells

We note that the short-circuit current density (I_{sc}) of the CIGS cell is greater than that of the CZTS cell because the absorption of light for short wavelengths by the CIGS material is greater than that of the CZTS material.

On the other hand, the open circuit voltage (V_{oc}) of the CIGS cell is lower than the CZTS cell (Table 4.9).

Parameters	Efficiency (%)	Fill Factor (%)	V_{oc} (V)	I_{sc} (mA/cm^2)
CIGS	19.0482	80.65293	0.61267	38.5486
CZTS	17.2928	84.93701	1.03621	19.6481

Table 4.9: Comparison between the optimal photovoltaic parameters of CIGS and CZTS solar cells.

4.7. Conclusion:

In this chapter, we presented the results of the numerical simulation by Atlas of CIGS and CZTS solar cells. We carried out the numerical simulation of those solar cells to calculate photovoltaic parameters such as efficiency. We have also optimized the CIGS and CZTS solar cells by studying the influence of thickness and concentration donors and acceptors of their layers to obtain the highest efficiency of the solar cells studied.

GENERAL CONCLUSION

In this work, we studied the electrical characteristics of the solar cell a heterojunction, ZnO/CdS/CIGS and ZnO/CdS/CZTS. Or the ZnO layer is used as a window layer, the CdS layer as a buffer layer and the CIGS and CZTS layers are the absorber layers, we used the digital simulation using Silvaco software, to study the characteristics of these devices. We also optimized the structure layer parameters such as the thickness and concentration of the doping to obtain electrical conversion efficiency maximum. We studied the effect of the two layers CZTS and CIGS on the performances of the solar cell (efficiency, fill factor, Voc, Jsc) . we fixed the CdS doping concentration and thickness at specific values because our analysis showed that varying these parameters had minimal impact on the overall performance of both CdS/CIGS and CdS/CZTS solar cells. We are then interested in doping and thickness layers in CZTS and CIGS to see their influences on the electrical efficiency of the structure.

Firstly, we found the simulation results of the solar cell in ZnO/CdS/CIGS: The short circuit current density jsc = 38.54 , the tension in open circuit Voc = 0.61 V, the form factor ff = 80.65% and the efficiency of conversion ɳ = 19.04%. These values are in agreement with those found experimentally.

Secondly, we compared the simulation results of the solar cell in ZnO/CdS/CIGS with the results of the ZnO/CdS/CZTS solar cell, the results of this last are as follows: The short-circuit current density jsc = 19.64 , there open circuit voltage Voc = 1.03 V, the form factor ff = 84.93% and the efficiency conversion ɳ = 17.29%. These results prove that the CIGS cell is the best.

This study allowed us to optimize the electrical efficiency of the solar cell and to show the impact of the CIGS and CZTS layers on the performance of the device according to the role of each of them.

As perspectives, we can delve deeper into studying various parameters, such as mobility, resistivity, bandgap, and potential defects, to gain a more comprehensive understanding of the material properties. Additionally, exploring different absorber layer materials could lead to the discovery of more efficient or cost-effective alternatives, for example: CdTe. Another approach involves modeling the studied solar cells using real experimental parameters, which would enhance the accuracy and relevance of the simulations. Furthermore, comparing the simulation results obtained by Silvaco-Atlas TCAD software with those from other simulation tools, such as SCAPS, can provide valuable insights and validate the findings, ensuring robustness and reliability in the conclusions drawn from the studies.

REFERENCES

[1] “NCERT authors, „Chapter Fourteen: Semiconductor electronics: materials, devices and simple circuits‟, in PhysicsTextbook: Class 12, 2014th ed., National Council of Education Research and Training, 2014, pp. 468–512.”.

[2] D. A. Neamen *et al.*, “Semiconductor Physics and Devices McGraw-Hill Higher-Education Library of Congress Cataloging-in-Publication Data,” 2003.

[3] H. Slide, “Modern Semiconductor Devices for Integrated Circuits (C”.

[4] R. S. Kapadnis *et al.*, “Cadmium Telluride/Cadmium Sulfide Thin Films Solar Cells: A Review,” *ES Energy and Environment*, vol. 10, pp. 3–12, Dec. 2020, doi: 10.30919/ESEE8C706.

[5] I. Bouchama, B. Mohamed, and Z. Heythe, *Effect of the buffer layer in CIGS-based Tandem solar cells*. 2017. doi: 10.13140/RG.2.2.19958.96324.

[6] W. N. Shafarman, S. Siebentritt, and L. Stolt, “Cu(InGa)Se2 Solar Cells,” *Handbook of Photovoltaic Science and Engineering*, pp. 546–599, Mar. 2011, doi: 10.1002/9780470974704.CH13.

[7] C. Roger, “Developpement de cellules photovoltaïques à base de CIGS sur substrats métalliques”, Accessed: May 02, 2024. [Online]. Available: https://theses.hal.science/tel-00965592

[8] S. Kalache, “Etude par simulation numérique d'une cellule solaire en CIGS.” Accessed: May 02, 2024. [Online]. Available: https://www.academia.edu/33756712/Etude_par_simulation_num%C3%A9rique_dune_cellule_solaire_en_CIGS

[9] S. Jung, S. J. Ahn, J. H. Yun, J. Gwak, D. Kim, and K. Yoon, “Effects of Ga contents on properties of CIGS thin films and solar cells fabricated by co-evaporation technique,” *Current Applied Physics*, vol. 10, no. 4, pp. 990–996, Jul. 2010, doi: 10.1016/J.CAP.2009.11.082.

[10] “H. Katagiri, K. Jimbo, S. Yamada, T. Kamimura, K. Maw, T. Fukano, T. Ito, and T. Motohiro, ‘Development of CZTS-based thin film solar cells,’ Solar Energy Materials and Solar Cells, vol. 65, no. 1-4, pp. 141-148, 2001.”.

[11] “K. Tanaka, N. Moritake, and H. Uchiki, ‘Cu2ZnSnS4 thin film solar cells prepared by non-vacuum processing,’ Solar Energy Materials and Solar Cells, vol. 95, no. 1, pp. 838-842, 2011.”.

[12] “S. Chen, X. G. Gong, A. Walsh, and S.-H. Wei, ‘Intrinsic point defects and complexes in the quaternary kesterite semiconductor Cu2ZnSnS4,’ Physical Review B, vol. 81, no. 24, p. 245204, 2010.”.

[13] “K. Ito and T. Nakazawa, ‘Characterization of Cu2ZnSnS4 thin films prepared by sulfurization of stacked metallic layers,’ Japanese Journal of Applied Physics, vol. 51, no. 10S, p. 10NC31, 2012.”.

[14] “J. T. Watjen, J. Engmann, S. Zander, M. C. Lux-Steiner, and K. J. R. Heinemann, ‘Optical properties of Cu2ZnSn(S,Se)4 solar cell absorbers and their impact on device performance,’ Journal of Applied Physics, vol. 105, no. 8, p. 086106, 2009.”.

[15] P. Y. Yu and M. Cardona, “Fundamentals of Semiconductors: Physics and Materials Properties, 4th Edition”.

[16] “P. Bhattacharya, Semiconductor Optoelectronic Devices, 2nd ed. Prentice Hall, 1996.”.

[17] “F. C. Krebs, Solar Cells: Materials, Manufacture and Operation, 1st ed. Elsevier Ltd, 2005. ”.

[18] S. M. Sze and M. K. Lee, “3RD EDITION Semiconductor Devices Physics and Technology”.

[19] T. L. Chu and S. S. Chu, “Thin film II–VI photovoltaics,” *Solid State Electron*, vol. 38, no. 3, pp. 533–549, Mar. 1995, doi: 10.1016/0038-1101(94)00203-R.

[20] W. Dib, “Modelisation des structures photovoltaïques : Aspects fondamentaux et appliques,” Dec. 2010, Accessed: May 26, 2024. [Online]. Available: http://dspace1.univ-tlemcen.dz//handle/112/697

[21] “ATHENA User’s Manual 2D Process Simulation Software,” 1990, Accessed: May 25, 2024. [Online]. Available: http://www.silvaco.com

[22] “ATLAS User’s Manual device Simulation Software,” 2004, Accessed: May 25, 2024. [Online]. Available: www.silvaco.com

[23] I. MALLEM, “Simulation des cellules solaires hétérojonction Si-SiGe par SILVACO.,” 2014.

[24] S. Kumar Padhy, “Effects of finger width & finger spacing on the electrical performance of W/CDS based MSM photodetector master of technology in VLSI design and embedded systems,” 2015.

[25] I. BENACER, “Modélisation des transistors organiques,” Apr. 2016.

[26] H. Amar, “Propriétés électriques de cellule solaire à base de diSéléniure de Cuivre Indium Galium CuIn(1−x)GaxSe2 (CIGS),” 2014.